HORIZON 2020 RESEARCH AND INNOVATION FRAMEWORK PROGRAMME OF THE EUROPEAN ATOMIC ENERGY COMMUNITY

HORIZON 2020

Nuclear Fission and Radiation Protection 2018 (NFRP-2018-4)

Project acronym: **SANDA**

Project full title: **Solving Challenges in Nuclear Data for the Safety of European Nuclear facilities**

Grant Agreement no.: **H2020 Grant Agreement number: 847552**

Workpackage N°: **WP2**

Identification N°: **D2.3**
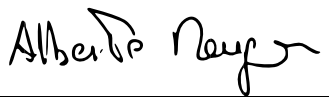
Type of document: **Deliverable**

Title: **Report on the $^{23}9Pu(n,\gamma)$, $^{92,94,95}Mo(n, \gamma)$ cross measurements at n_TOF and GELINA**

Dissemination Level: **PU**

Reference:

Status: **VERSION 1**

Comments:

	Name	Partner	Date	Signature
Prepared by:	A. Mengoni	8	22-06-2024	*Alberto Mengoni*
WP leader:	D. Cano-Ott	1	22-06-2024	*<If at all possible use electronic signature>*
IP Co-ordinator:	E. González	1	22-06-2024	

Executive summary

The NEA/OECD included the cross-section of neutron capture and neutron-induced fission reactions for ^{239}Pu in its High Priority Request List, in response to the demands for more accurate and reliable nuclear data essential for the design and operation of nuclear technologies. Recent efforts have been concentrated on meeting these data needs by means of a new measurement utilizing ^{239}Pu samples in the n_TOF time-of-flight facility at CERN.

Ten thin samples of 1 mg each were deposited within a novel ionization chamber, specifically designed for the challenging conditions of high counting rates coming from the α-decay of ^{239}Pu. This fission fragment detector was operated in combination with the n_TOF Total Absorption Calorimeter to highly suppress the γ-ray fission background in the measurement of the capture reaction cross-section, employing the so-called fission tagging technique. To extend the measurement of the capture cross-section, a thicker ^{239}Pu sample of 100 mg was also used.

The analysis of the measurement has finished recently. The achieved uncertainties in the results are very similar to those expected from the calculations performed in the preparation of the measurement. The obtained results have an unprecedented energy resolution and will allow to improve the present ^{239}Pu cross section evaluations.

Cross-sections for neutron-induced reactions with molybdenum is relevant in various scientific fields ranging from nuclear astrophysics to nuclear technologies. In addition to its astrophysical role, molybdenum isotopes can be found in fission power plants as fission products and the use of this material is under study for future improved reactors.

Molybdenum is found in pre-solar silicon carbide grains and an accurate knowledge of its neutron capture cross section plays a crucial role in constraining stellar nucleosynthesis models, particularly for AGB stars. A deviation in the model predictions of isotopic composition in SiC grains has been observed when using Mo cross-section data from the two main KADoNiS versions. Nevertheless, experimental data for the neutron capture cross-section found in the literature for Mo isotopes suffer from large uncertainties. This is also reflected in the large uncertainties of the cross sections recommended in the ENDF/B-VIII.0 library and in the uncertainty of the MACS found in the KADoNiS database, which is of the order of 10% at 30 keV.

Therefore, a new set of measurements of ^{94,95,96}Mo(n, γ) reaction was performed at the n_TOF time-of-flight facility at CERN (Switzerland). In addition, to reduce systematic uncertainties and improve accuracy in the resonance parameters additional transmission measurements were performed at the GELINA time-of-flight facility located at the JRC-Geel (Belgium).

This report is split into two parts:

PART I: Measurement of the ^{239}Pu(n,γ) cross-section measurement at n_TOF

PART II: ^{94,95,96}Mo (n,γ) and (n,tot) measurements

Table of contents

PART I: Measurement of the ^{239}Pu(n,γ) cross-section at CERN n_TOF

V. Alcayne[a], J. Andrzejewski[b], D. Cano-Ott[a], T. Cardinaels[c], P. Dries[c], A. Gawlik[b)], E. González-Romero[c], J. Heyse[d], G. Leinders[c], T. Martínez[a], E. Mendoza[a(*)], A. Moens[d], A. Pérez de Rada[a], J. Perkowski[b], A. Plompen[d], C. Paradela[d], A. Sánchez-Caballero[a], P. Schillebeeckx[d], G. Sibbens[d], K. Van Hecke[c], K. Vanaken[c], D. Vanleeuw[d], K. Verguts[c], M. Verwerft[c], R. Wynants[c], and the n_TOF Collaboration[e]

[a]*Centro de Investigaciones Energéticas Medioambientales y Tecnológicas (CIEMAT), Spain.*
[b]*University of Lodz, Pomorska 149/153, Lodz, 90-236, Poland*
[c]*SCK CEN, Belgian Nuclear Research Centre, Boeretang 200, Mol, B-2400, Belgium*
[d]*European Commission, Joint Research Centre (JRC), Retieseweg 111, Geel, B-2440, Belgium*
[e] *www.cern.ch/n_TOF*

(*) corresponding author: emilio.mendoza@ciemat.es

1   Introduction to Part I

As the usage and development of nuclear technologies continue to expand, so does the demand for precise and reliable nuclear data. In particular, more accurate neutron-induced fission and capture cross-section data for ^{239}Pu are required for the design of novel critical nuclear systems, such as Generation-IV reactors [1] and Accelerator Driven Systems (ADS), and for the operation of current thermal reactors loaded with mixed oxide (MOX) fuels. Due to the limited experimental data available and the discrepancies among the main evaluated nuclear databases [2][3][4][5][6], new measurements of the capture and fission cross-section of ^{239}Pu are highly recommended, as it is included in the NEA/OECD High Priority Request List [7].

Only two measurements of the ^{239}Pu capture cross-section have been reported with enough energy resolution to perform a reasonable resonance analysis in the resolved resonance region. The first one was performed by Gwin et al. [8] in 1971, covering the neutron energy range between 0.02 eV and 30 keV. The second one was performed in 2014 by Mosby et al. [9][10][11] at the Los Alamos Neutron Science Center using the DANCE detector, for neutron energies from 10 eV to 1.3 MeV. In the latter, only the shape of the cross-section was measured, i.e. it was normalized to the ENDF/B-VII.1 [6] cross section at 17-18 eV.

In this work, a new recent measurement of the ^{239}Pu capture and fission cross-section performed at the neutron time-of-flight facility n_TOF [12] at CERN is presented. The experiment was performed in the 185 m experimental area EAR1. This flight path is nearly 10 times larger than the ones used for previous ^{239}Pu capture measurements, enabling a potential improvement in the energy resolution of the measured cross-sections. To accomplish this, the collaborating groups have made use of the expertise obtained in previous capture measurements of fissile samples [13][14] to design a new improved experimental setup, which consists in the simultaneous operation of the n_TOF Total Absorption Calorimeter (TAC) [15], already used in previous measurements, and a new fast Fission Fragment Detector (FFD) specifically fabricated for this experiment.

2   Experimental setup

2.1   The samples

Two different experimental configurations were used. First, ten thin samples and the FFD were used to efficiently subtract the fission background between 0.02 eV to 1 keV. Reaching higher neutron energies in this configuration, in the case of the capture cross-section, is limited by the low statistics and high background. For this reason, a thicker sample was utilized in the second experimental configuration without the FFD to reach higher neutron energies at least up to 10 keV (limited also by the gamma-flash effect in the BaF_2 crystals of the TAC).

Therefore, a total of 11 PuO_2 samples were manufactured at the European Commission Joint Research Centre (JRC-Geel, Belgium) for this experiment. Ten samples, each of them with a mass lower than 1 mg, were deposited in aluminum foils with 10 µm thickness (see left picture in Figure 1) and hold by aluminum rings that were placed inside the fission chamber.

Figure 1 Left: picture of the mounting process of one PuO₂ sample in the fission chamber. Right: picture of the actual capsule containing the thick sample during its mounting between two aluminum rings with kapton and mylar foils (the top mylar ring does not appear in this picture).

Target position	Activity (MBq)	Mass (µg)	Areal density (µg/cm²)
1	2.24	975	310
2	2.22	965	307
3	2.20	959	305
4	2.09	911	290
5	0.28	122	39
6	1.94	844	268
7	2.19	953	303
8	2.11	920	293
9	2.09	912	290
10	2.25	982	312

Table 1 Properties of the ²³⁹Pu targets inside the fission chamber used in the n_TOF experiment.

Some physical properties of these samples are shown in Table 1. Additionally, a thicker target of 101.69 mg was produced and encapsulated in a two-piece hat-shaped aluminum structure (see Figure 1, right image). The hat-shaped structure minimizes the possible movements of the sample powder inside the capsule. The same adhesive used to join these two pieces was utilized for another identical aluminum capsule without plutonium, which was necessary for the background characterization in dedicated measurements.

2.2 The fission fragment detector

The new FFD is a multi-section ionization fission chamber. Its main purpose is to serve as a veto for fission events registered in the TAC. In addition, the FFD was used to measure the ^{239}Pu(n,f) cross-section.

The design of the FFD was optimized to ensure: i) a good discrimination between alpha particles coming from the radioactive decay of ^{239}Pu(n,f) and the fission fragments emitted in the nuclear fission reactions, ii) a high time resolution to minimize pile-up effects mainly due to the high counting rate from the alpha-decays (around 106 counts/s), and iii) as high a fission detection efficiency as possible, determined by the restrained dimensions to fit within the 10 cm inner radius of the TAC (see right image in Figure 2).
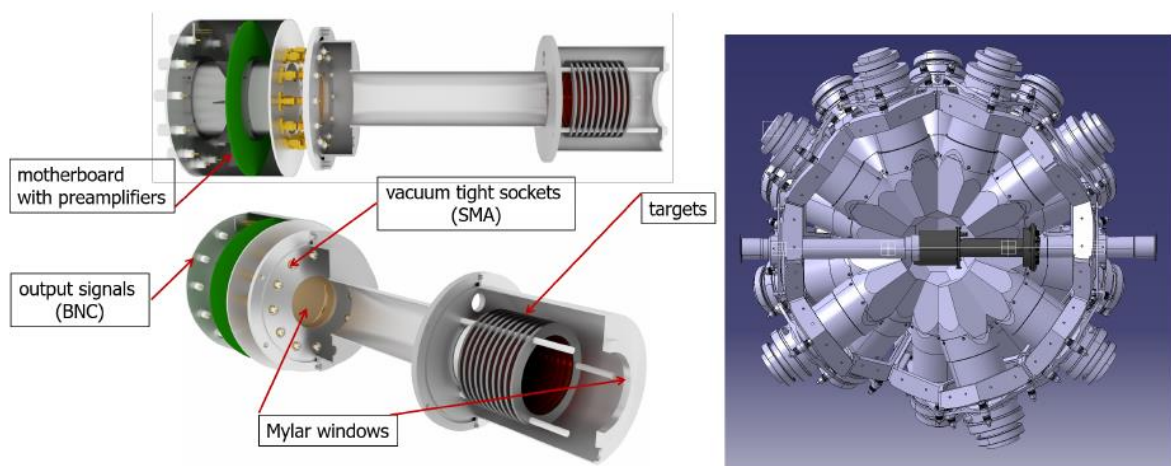

Figure 2: Left: a simplified 3D model of the fast fission fragment detector with the attachable aluminum box which houses the motherboard with the preamplifiers. Some critical elements inside the chamber, such as the aluminum electrodes or cables are omitted. Right: a 3D model of the fast fission fragment detector mounted inside the TAC. One half of the TAC is hidden for visualization purposes. The neutron beam would be coming from left in the image.

The ten ^{239}Pu targets were placed on the cathodes of ten parallel plate ionization detectors arranged within a cylindrical chamber. This design eliminates potential cross-talk or interdependence between plates, enabling separately detection of the fission fragments from each target. A gas mixture of 90% Ar and 10% CF_4 continuously flows through the chamber, selected to provide the shortest rise times of the registered signals.

An aluminum box containing some electronics is placed outside the central space but still inside the TAC assembly structure, and is attached to the FFD, as can be seen on the left hand side of the left image in Figure 2. This chamber contains the necessary preamplifiers to obtain the desired properties for the electrical signals. Following these preamplifiers, the signals go through an analogue fast amplifier before reaching the n_TOF digitalization system [16].

An identical dummy fission chamber was built without the plutonium targets to characterize the beam-related background of the measurement. This dummy chamber was also used, after some

modifications, as the supporting structure of the thick sample for the second experimental configuration.

2.3   Description of the experimental setups

As previously mentioned, two different experimental setups were used. In the first configuration, both the TAC and the FFD were utilized to simultaneously measure the capture and fission cross-section of ten [239]Pu thin samples, housed within the main chamber of the FFD.

To measure capture, the fission tagging technique [17] was employed by detecting fission events with the FFD, thereby determining the γ-ray fission background registered in the TAC crystals. Due to the neutron sensitivity of BaF_2 crystals, a Li-doped polyethylene neutron absorber was built to minimize the neutron background originating from fission and scattering processes. The neutron absorber comprises two matching halves, with the interior tailored to the geometry of the FFD chamber (see left picture in Figure 3 which shows one half being installed).

Figure 3: Photographs of the experimental setup of the [239]Pu measurement at n_TOF. Left: mounting of the Li-doped polyethylene neutron absorber surrounding the FFD, located at the center of the TAC. Middle: modified version of the dummy fission chamber with the thick plutonium sample for the second experimental configuration, before mounting inside the TAC. Right: top view of the [239]Pu thick sample in the modified dummy fission chamber.

In the second experimental configuration, the encapsulated thick [239]Pu sample was employed for measuring the capture cross-section above 1 keV with the TAC. Positioning the sample within the beam trajectory while maintaining stability, alignment, and minimizing dead material effects, was done by using the dummy fission chamber. To mitigate background from the dead material of the dummy FFD, some elements such as cables, aluminum plates, structural pieces, etc. were removed, as they are not necessary for this configuration. This new version of the dummy fission chamber (without the aluminum cap for visualization purposes) is displayed in the middle image of Figure 3.

The thick sample was placed in a fixed position corresponding to the estimated center of the TAC. A top view of the encapsulated sample in its definitive position within the chamber can be seen in the right image of Figure 3.

The assembly process was similar to the first configuration, including the same neutron absorber shown in the left image of Figure 3.

3 Data analysis

3.1 Pulse shape analysis routine

We have developed a new pulse shape analysis routine for this measurement. The work has been focused in improving the performance of the pile-up reconstruction. Examples of digitized signals together with the pulse shape reconstruction are provided in Figure 4.

This new routine has been tested and compared with the previous one used for the TAC. The intention is to use it also for future measurements.
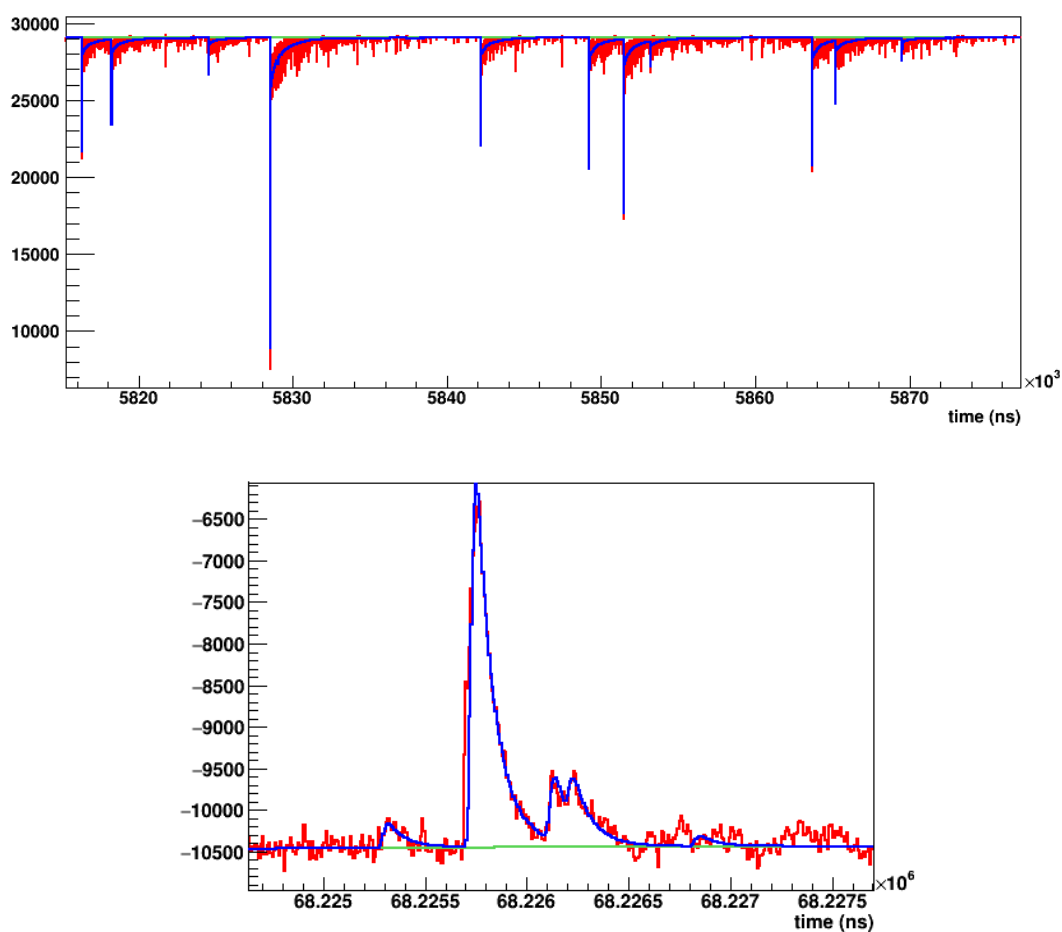

Figure 4: In red, digitized signals from the TAC (top) and from the FICH (bottom), together with the resulting fits provided by the pulse shape analysis routine, in blue.

3.2 Neutron flux

The neutron flux or fluence in the measurement has been determined in the following way. We have first obtained the energy dependency of the neutron beam from the so called silicon monitor (SiMon)

placed on de beam during the entire measurement. This detector contains a ^{6}Li foil which covers the full neutron beam, and measures the (n,t) reactions in it.

The result of this measurement provided us the neutron flux of the full beam. However, the ^{239}Pu samples cover only a fraction of the beam. This fraction is quite constant with the neutron energy in the eV and keV region, but not below 1 eV nor above 1 MeV. For this reason, the final flux has been obtained by modifying the measured one with information provided by FLUKA simulations and from measurements with Au samples of different diamteters.

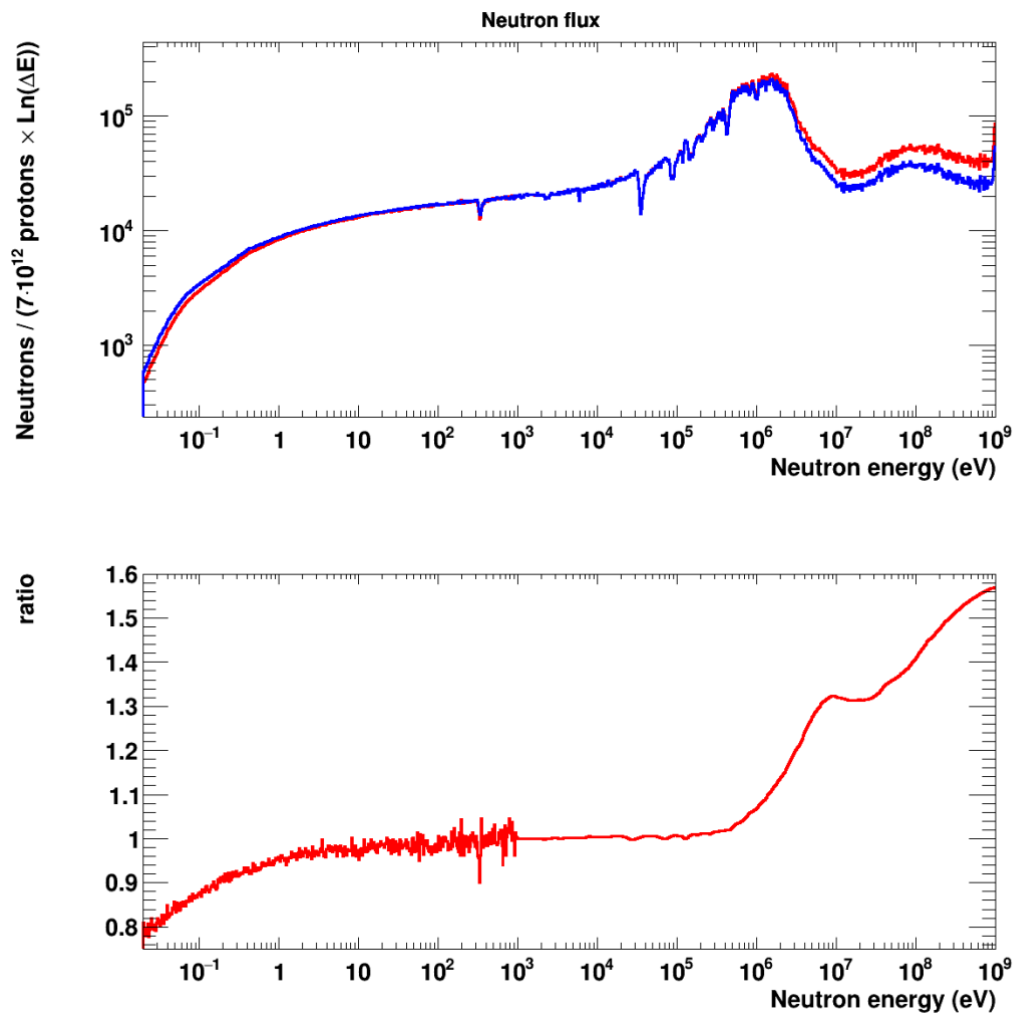The resulting neutron flux us presented in Figure 5.

Figure 5: Top: In red, neutron fluence of the full beam, as a function of the neutron energy, at n_TOF EAR1 during the ^{239}Pu measurement. In blue, the neutron fluence hitting a 2 cm diameter sample, normalized to the red curve in the eV region. Bottom: ratio between the fluences provided in the top panel.

3.3 Analysis of the FICH

The data from the fission chamber has been analyzed with the new pulse shape analysis routine. One of the more challenging characteristics of the measurement is the high activity of ^{239}Pu, which is ~2 MBq/mg, which corresponds with ~2 MBq in each of the ten ^{239}Pu samples (see Table 1). This induces a non-negligible amount of pulse pile-up, but the routine was able to resolve it effectively.

An example of amplitude spectra in the FICH is presented in Figure 6. The two graphs there correspond to the amplitude spectra with the beam on (red) and beam off (blue) of the FICH in time of flights corresponding to neutron energies between 0.2 and 0.4 eV. This energy range was chosen to cover the strongest resonance of ^{239}Pu at 0.3 eV.

In absence of neutrons, the spectra corresponds to the detection of α-particles from the decay of ^{239}Pu. When the neutron beam is turned on, the fission fragments appear together with the α-particles. Since they have more kinetic energy, they appear at higher amplitudes. As shown in Figure 6, in this detector there is an excellent separation between the α-particles and the fission fragment. This allows to discriminate both type of particles with a threshold, without reducing significantly the fission detection efficiency.
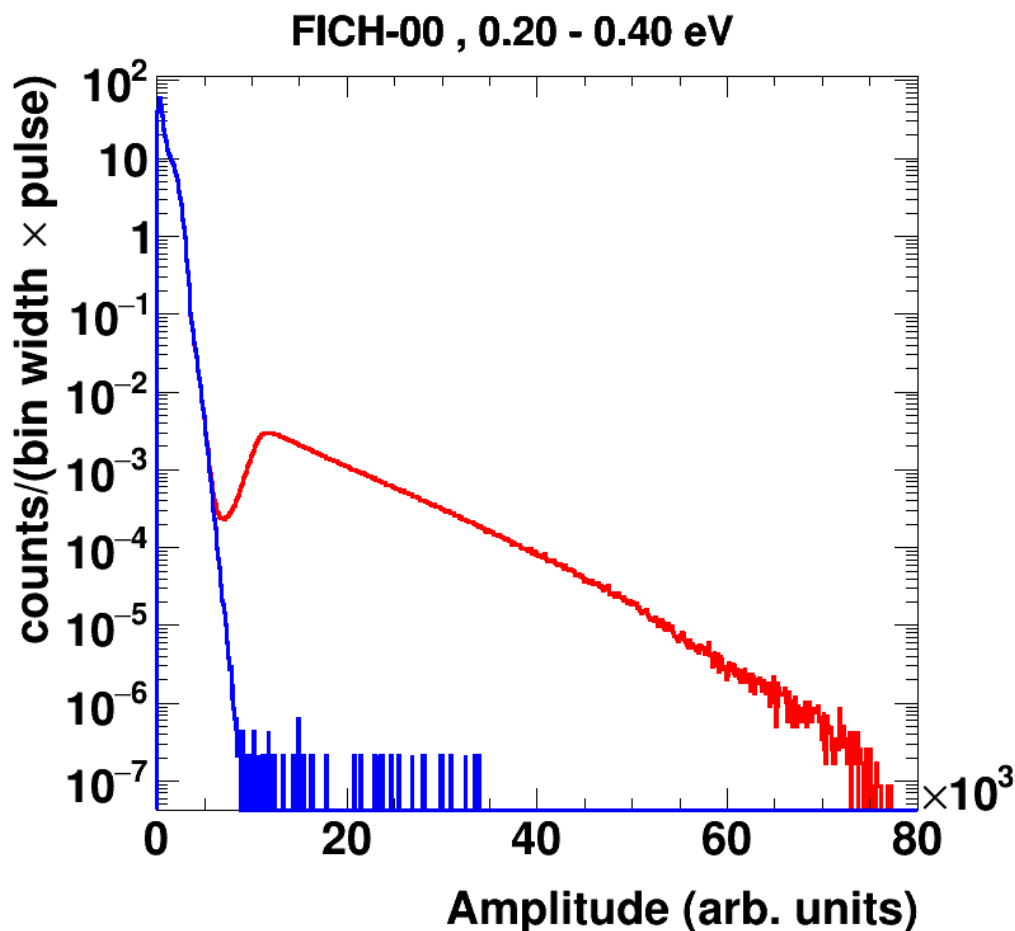

Figure 6: Amplitude spectra in the FICH close to the 0.3 eV strongest ^{239}Pu resonance. In red, in a beam on experiment; and in blue, with the beam off. An excellent separation between alpha particles (blue) and fission fragments (red) can be observed.

3.4 Fission yield

With an appropriate threshold the α-particles are removed from the analysis keeping an efficiency of 89%. Since there are no backgrounds the fission yield is then easily obtained from the counting rates and the neutron fluence. The obtained fission yield is compared with the most recent evaluation of [239]Pu provided by the IAEA-INDEN project in Figure 7. They have been normalized in the 9-20 eV energy region. Both yields seem to be compatible within a few percent in the whole energy region of the measurement, which goes from 0.02 eV up to 20 MeV. This corresponds to nine orders of magnitude in neutron energy; and this is the first measurement (at least publicly available) covering such a wide energy range.
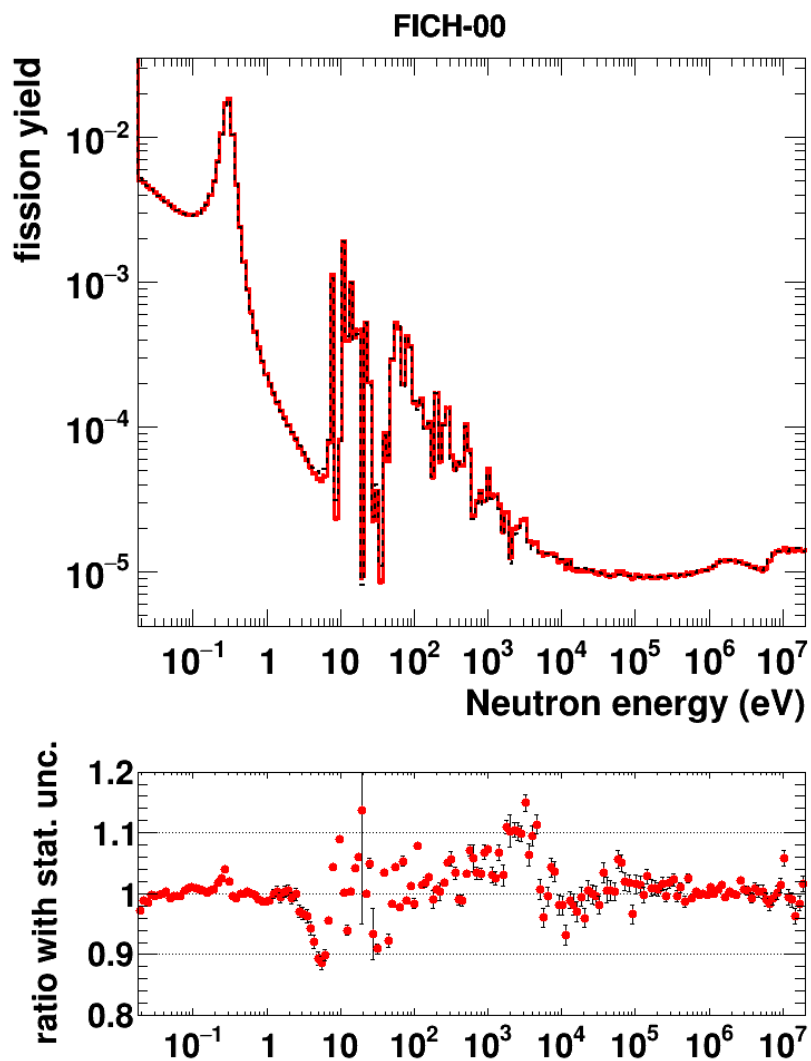

Figure 7: Top: [239]Pu fission yield measured at n_TOF (red), compared with the most recent evaluation of the IAEA-INDEN project (black). Bottom: ratio between the two yields on the top.

3.5 Detection efficiency of the TAC

The detection efficiency of the TAC has been obtained from detailed Monte Carlo calculations, as in previous works [18][19], using the Geant4 Monte Carlo toolkit [20][21].

For the geometry of the experimental setup we have used for the TAC the same we used in previous analysis [22]. The geometry of the FICH, the samples and the neutron absorber have been developed specifically for this analysis. We show part of this geometry in Figure 8.
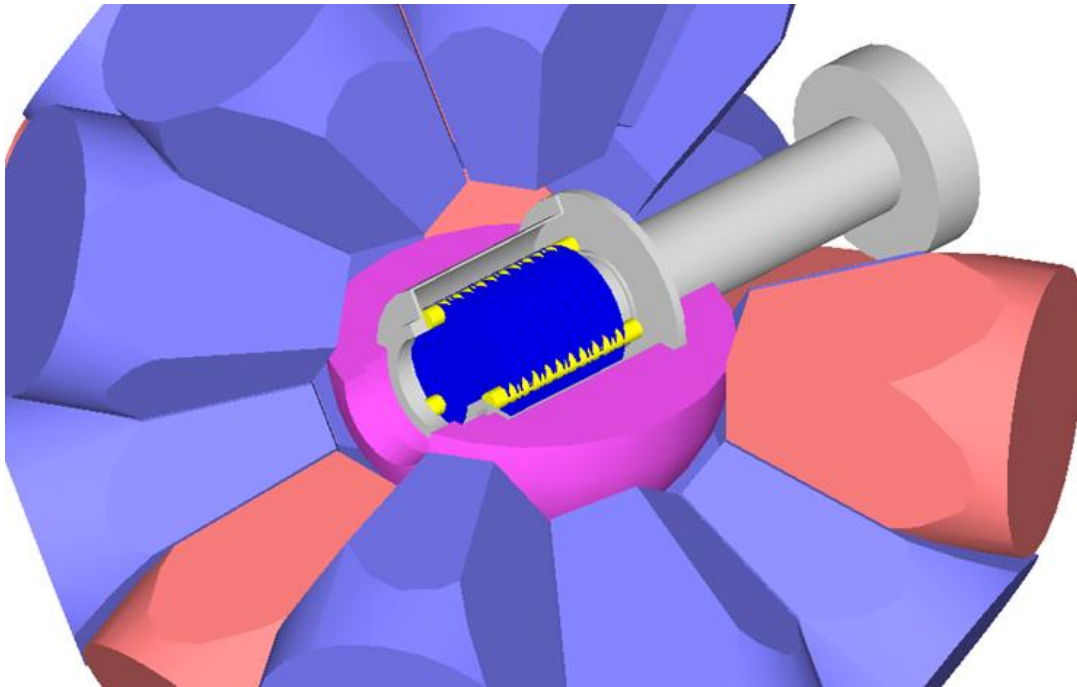

Figure 8: Part of the geometry of the experimental setup implemented in the Geant4 code to perform the Monte Carlo simulations.

One of the largest contributions to the total uncertainty of the capture cross section and the alpha ratio is the one due to the capture detection efficiency. For this reason, we performed a great effort in this task.

The Monte Carlo code has been validated with measurements performed with calibration sources, first, and then with measurements performed with a [197]Au sample. After verifying that the code was capable of reproducing all these measurements, we began to study the [239]Pu(n,γ) cascades. These have been produced with the NuDEX code [23]. The parameters of the cascade model have been adjusted to reproduce the experimental spectra. After the adjustment procedure, we were able to reproduce the experimental results with high accuracy, as shown in Figure 9 and Figure 10.
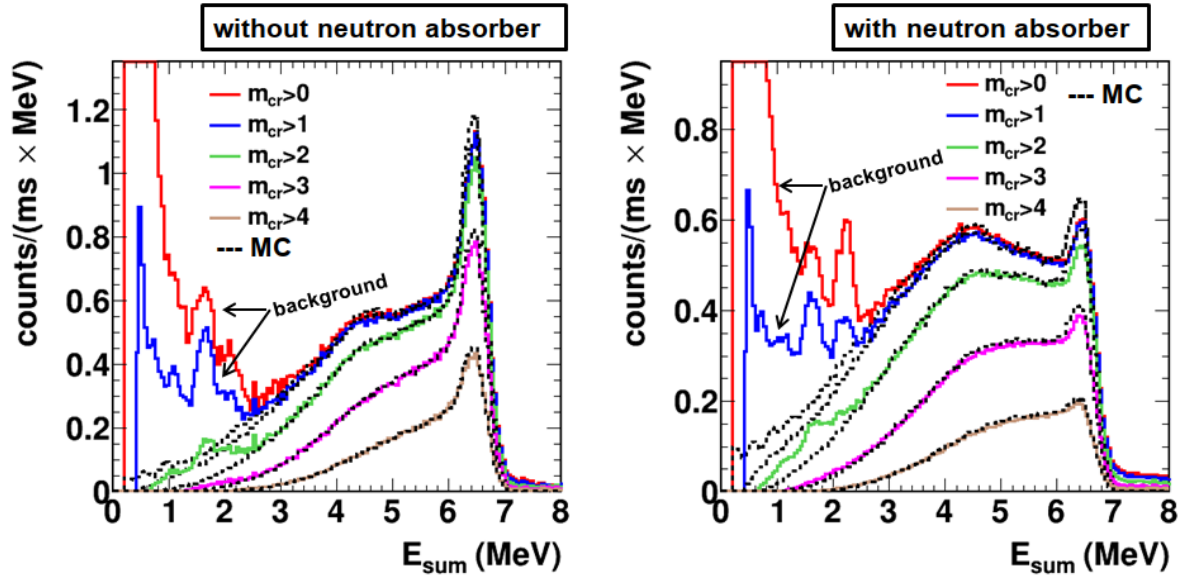
Figure 9: Deposited energy spectra in the TAC for 0.2-0.4 eV due to ^{239}Pu(n,γ) cascades without (left) and with (right) the neutron absorber in place. The solid lines correspond to the experimental spectra, for different detection multiplicities (m_{cr}), and the dashed lines to the results of the Monte Carlo calculations.
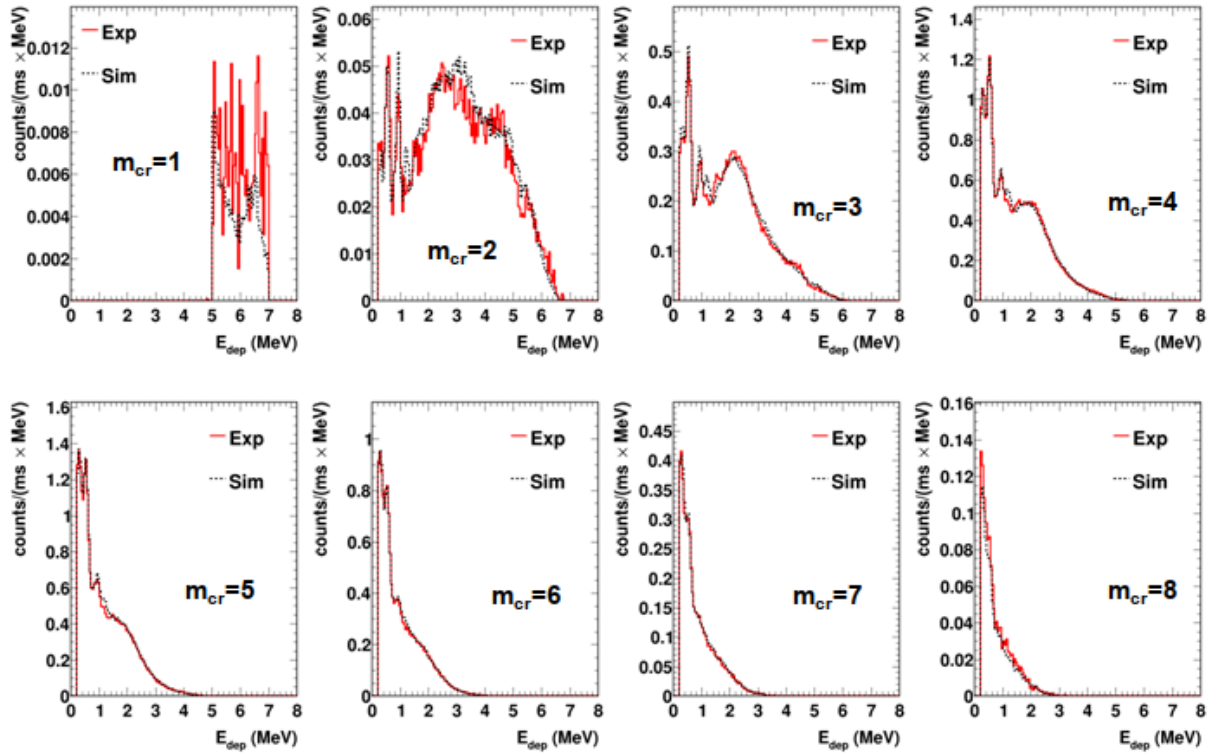

Figure 10: Comparison between experimental (red) and simulated (black) energy deposited spectra due to ^{239}Pu(n,γ) reactions, for 0.2-0.4 eV neutron energies, without neutron absorber. Here we show the individual crystal deposited energy spectra, gated when 5<E_{sum}/MeV<7 and different conditions in m_{cr}.

3.6 Time coincidences between the TAC and the FICH

The measurement with the FICH is performed in coincidence with the TAC. In Figure 11 we show the distribution of time differences between both detectors. The peak in the center, close to 0, corresponds to events detected at the same time in both detectors (i.e. fission reactions mainly). The flat structure on the left of this peak corresponds to random coincidences. The tail on the right corresponds to events which have been detected in the TAC tens or hundreds of ns after the fission reaction, and are mainly due to neutrons from fission reactions.
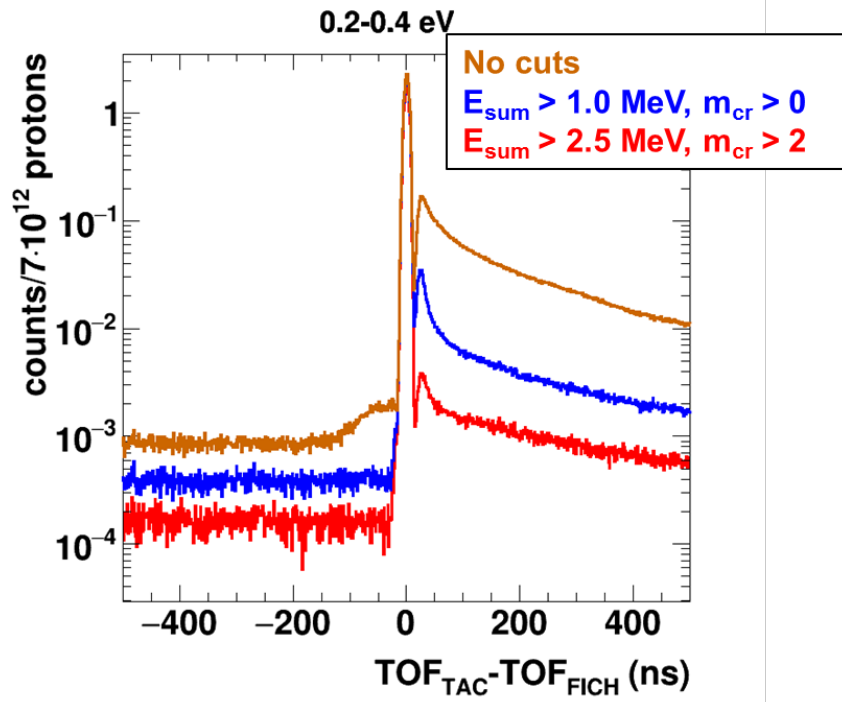

Figure 11: Distribution of time differences between the TAC and the FICH, for different conditions in the TAC events.

All the events in the TAC in coincidence with the FICH are considered to be due to fissions. Since the detection efficiency of the FICH is not 100% (is ~90%), there is still a remaining background which needs to be subtracted. On top of this, from Figure 11 it is also clear that there is some additional background to be subtracted, corresponding to the tail on the right, i.e. to some counts in the TAC which come tens or hundreds of ns after the fission reactions. We will refer here to this background component as post-fission background.

3.7 Post fission background

We have characterized the background in the TAC produced by fission reactions with a delay of tens of hundreds of ns (*post fission background*) by obtaining the total deposited energy spectra E_{sum} as a function of the time difference with respect to the FICH. This characterization allows to estimate this background component both in terms of deposited energy and time-of-flight spectra.

As an example we show the contribution of this type of background, together with other components, in Figure 12 (E_{sum} spectra) and Figure 13 (time of flight spectra). In Figure 12 we present the total E_{sum}

spectrum in the TAC in anticoincidence with the FICH in red. The remaining fission baclground appears in blue, the background not related with the neutron beam in green, the background related with the beam but not with the ^{239}Pu sample in magenta, and the post fission background in brown. All the spectra corresponds to neutron energies between 0.2 and 0.4 eV, i.e. in the strongest resonance of ^{239}Pu at 0.3 eV. When we subtract all these background components to the red spectrum, we obtain the spectrum in black, with the remaining detections which are supposed to be due to ^{239}Pu(n,γ) reactions. As it can be appreciated, the shape of the ^{239}Pu(n,γ) spectrum has the expected shape, which guarantees that the background subtraction is being performed properly. In particular, if the post fission background is not properly taken into account, the peak at ~9 MeV remains in the ^{239}Pu(n,γ) spectrum.

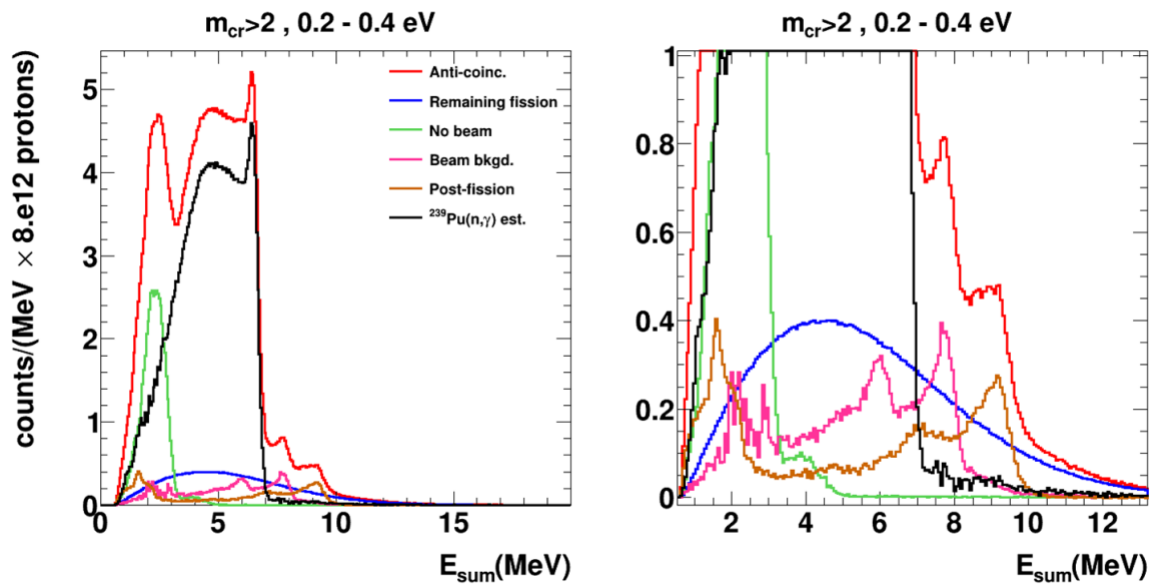**Figure 12: Total energy (E$_{sum}$) spectra in the TAC for neutron energies between 0.2 and 0.4 eV and m$_{cr}$>2. The total spectrum in anticoincidence with the FICH is presented in red; the different background components in different colors, and the spectrum due to capture in ^{239}Pu in black. The figure on the right is a zoom of the figure on the left.**

The contribution of the post fission background in the time-of-flight spectrum is shown in Figure 13. As expected, it has a shape similar to the (prompt) fission background, although it is not the same. Its size is ~10% of the fission background.
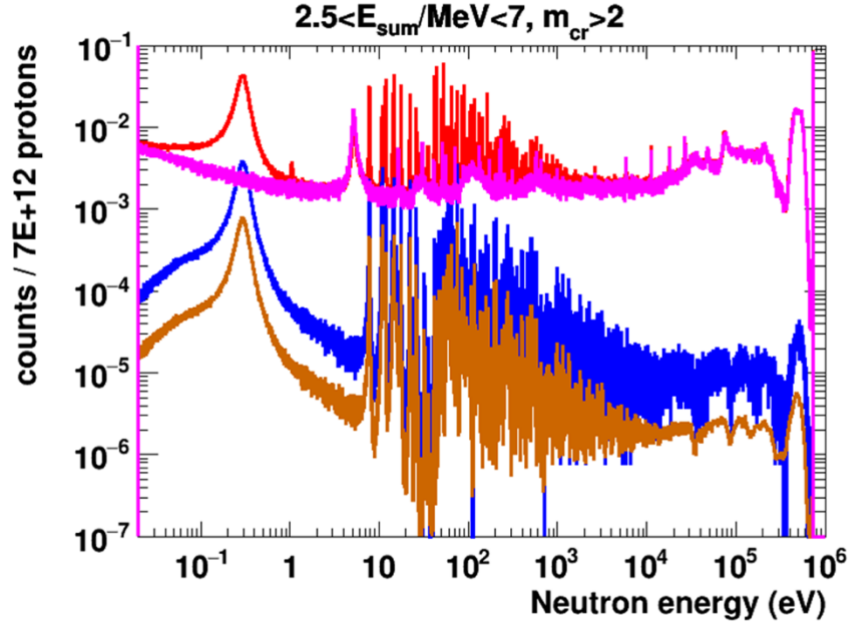
Figure 13: Time of flight spectra (2.5<E_{sum}<7 MeV and m_{cr}>2) for all the counts in the TAC in anticoincidence with the FICH (red), together with the background due to prompt (blue) and post (brown) fission.

3.8 Neutron sensitivity

We need to calculate the background due to elastic scattered neutrons in the sample. This is a quite complex background since it cannot be measured directly and also because its time-of-flight structure may be complex.

For these reasons, we have calculated this background component with Monte Carlo calculations, which have been verified with experimental results. The simulations have been performed using NuDEX in Geant4 to model the (n,γ) cascades. We have also performed simulations without NuDEX, for comparison purposes.

Some results are shown in Figure 14. The results from the simulations have not been normalized to the experimental data, which indicate that the estimation of the background is quite reliable. In any case, the contribution of this background to the total background is small and do not have a great impact in the obtained capture yield.
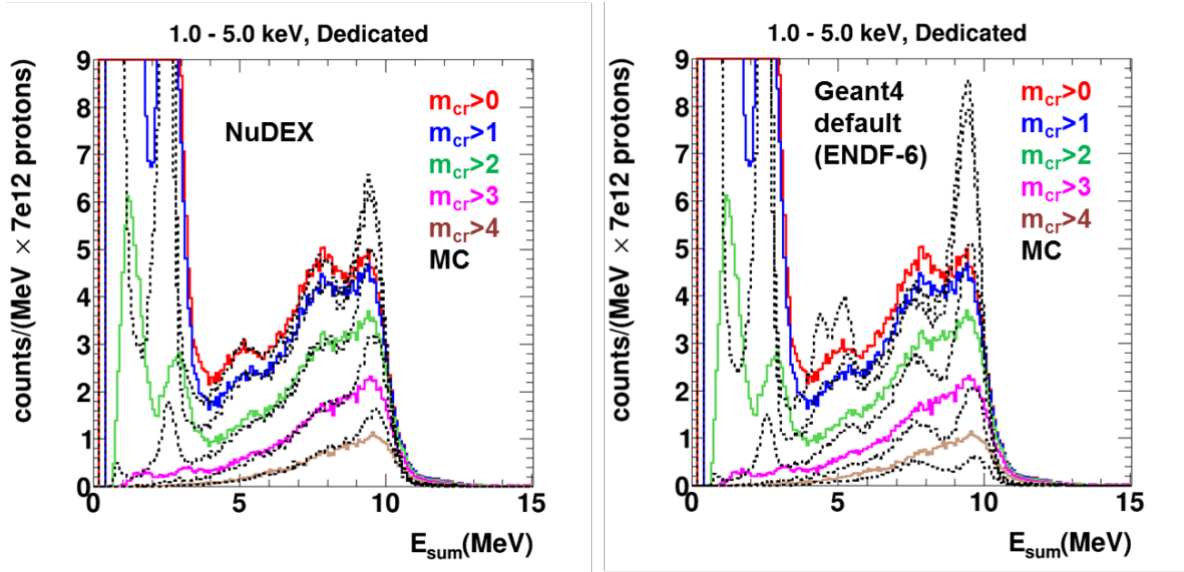
Figure 14: Deposited energy in the TAC when placing a graphite sample on the beam, in the 1-5 keV neutron energy interval. The different colors correspond to different conditions in m_{cr}. The solid lines are experimental results whereas the black dotted lines correspond to simulations performed with NuDEX (left) and without NuDEX (right).

3.9 Fission efficiency

The fission tagging efficiency has been determined by the ratio of deposited energy spectra between the total fission counts in the TAC and the fission counts that are tagged by the FICH (in coincidence). All the known backgrounds, except for the fission, have been subtracted. In Figure 15, the determined background excluding fission is drawn in light blue. In dark blue and red, the tagged fission and the total fission in the TAC, respectively.

As capture cannot be subtracted, the determination of fission efficiency is restricted to E_{sum} energies above the ^{240}Pu neutron separation energy (6.5 MeV). In addition, capture events can also be reduced by increasing the cut in the crystal multiplicity. In order to get a more robust calculation of the fission tagging efficiency, different thresholds in E_{sum} and m_{cr} have been used. For the E_{sum}, three lower thresholds have been used: 8, 10 and 13 MeV. The higher the threshold in E_{sum}, the less counts from other backgrounds different from fission that were not subtracted. However, increasing the E_{sum} also means reducing the statistics. Same happens with the lower threshold in the m_{cr}, which has been taken from 0 to 7. The efficiencies calculated by these different conditions on the data are represented in Figure 16. The statistical error of each value is also represented by the shaded area around the point of the same color. As can be observed, the values are in good agreement with each other within the errors regardless of the threshold used in both E_{sum} and m_{cr}. A slightly more dispersion is observed with E_{sum}>8 Mev, as expected as it is closer to the total absorption peak of the capture events and the post-fission background, that is also drawn in Figure 15 and shows a peak around 9 MeV.

The importance of the main background contributions to the calculation of the fission tagging efficiency has also been analyzed. The change, in percentage, on the efficiency value in the 0.3 eV resonance after a 1% change in the beam on related background (dummy) and the post fission background have been computed. Results show that the fission tagging efficiency is less sensitive to the dummy and post fission background as the restrictions on m_{cr} and E_{sum} are increased. The numbers

also show that the restriction $E_{sum} > 8$ MeV is around 10 times more sensitive to the post fission background than the next cut, as suggested also in Figure 15. Therefore, the $E_{sum} > 10$ MeV restriction seems to be the best option in terms of balance between statistics and reliability.

The results shown in the left panel of Figure 16 have been obtained from the first fission resonance at 0.3 eV, the one with the highest statistics and the best signal-to-background ratio. However, the fission tagging efficiency has also been calculated in the next few resonances, as shown in the right panel of Figure 16. The values calculated in these resonances are compatible with the 0.3 eV resonance, which serves to validate the method used.

Given all of the aforementioned information, the efficiency of fission tagging, along with its estimated uncertainty, is set to $\varepsilon_f = 0.894(5)$.
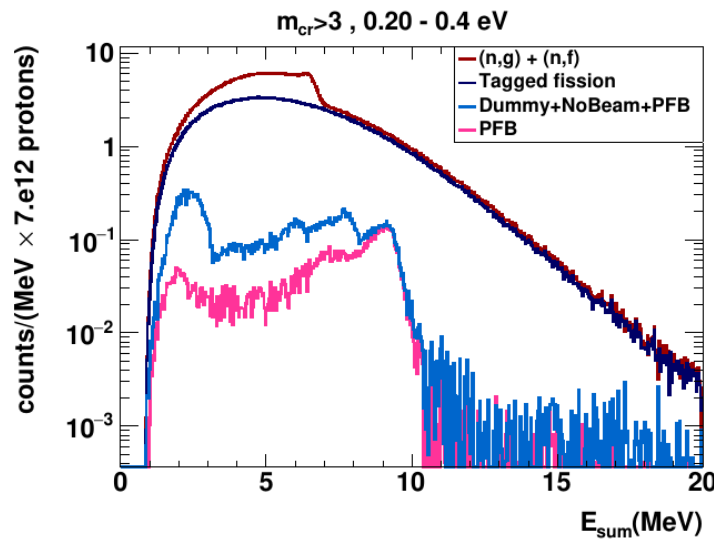

Figure 15: Total energy spectra in the TAC to illustrate the calculation of the fission tagging efficiency.
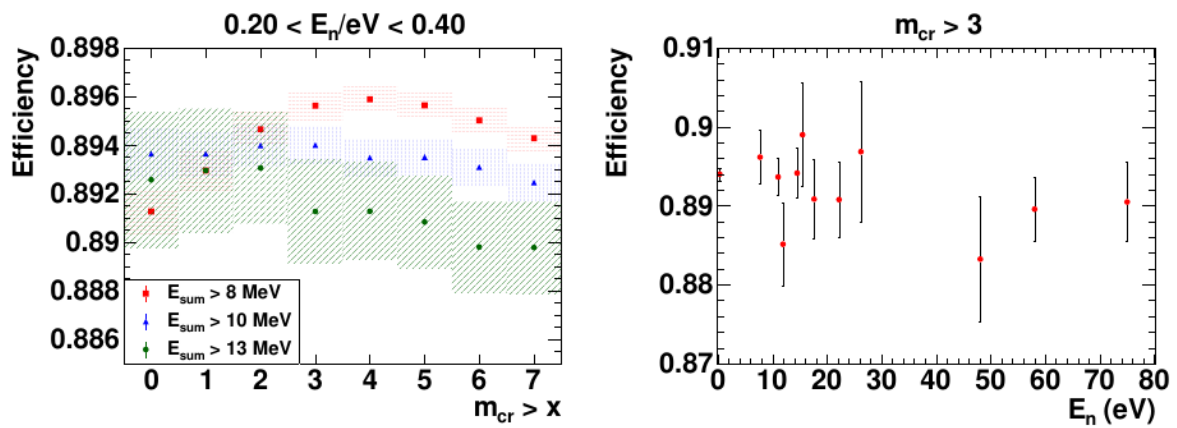

Figure 16: On the left, values of the fission tagging efficiency calculated with different lower thresholds on E_{sum} and m_{cr}. On the right, values calculated for different fission resonances.

4 Results

The capture yield Y_γ can be obtained in the experimental configuration performed with the FICH with [13]:

$$Y_\gamma = \frac{C_{aco} - \dfrac{1-\varepsilon_f}{\varepsilon_f} C_{tag} - C_{bkg*}}{\varepsilon_\gamma \cdot \phi}$$

where C_{aco} is the number of counts in the TAC detected in anticoincidence with the FICH, C_{tag} is the number of counts in the TAC detected in coincidence with the FICH, C_{bkg*} is the background not related to the (prompt) fission, ε_f is the detection efficiency of the FICH, ε_γ is the detection efficiency of the TAC, and ϕ is the number of neutrons hitting the sample. All the quantities but the efficiencies depend on the neutron energy.

In the thick sample configuration there is no fission fragment detector, and the yield is obtained with:

$$Y_\gamma = \frac{C_{tot} - C_{bkg}}{\varepsilon_\gamma \cdot \phi}$$

where C_{tot} is the total number of counts in the TAC and C_{bkg} is the background, including fission in this case.

The ^{239}Pu capture cross section σ_γ is obtained from the yield afterwards since:

$$Y_\gamma = \frac{\sigma_\gamma}{\sigma_{tot}} (1 - e^{-n \cdot \sigma_{tot}})$$

where σ_{tot} is the total cross section and n is the number of atoms per unit surface.

Section 3 describes how we have obtained all the quantities needed for the capture yield: the neutron flux (section 3.2), the detection efficiencies (sections 3.5 and 3.9), and the different background components (sections 3.7 and 3.8). The normalization of the capture yield has been performed to the fission cross section of ^{239}Pu between 9 and 20 MeV in the INDEN evaluation [24] (July 2023 version).

We show the resulting yield in Figure 17 to Figure 22 compared to the ENDF/B-VII.1 data library. As it can be observed, differences between our results and the evaluated ones are not big, but quite sizeable in some of the resonances.

In those figures it can also be appreciated how some deeps appear at certain energies. The deeps correspond to resonances of Ag, which are visible in both the measurement with the ^{239}Pu sample in place and with the dummy fission chamber in place. We attribute the appearance of these resonances to the Ag content present in the electronics of the FICH. The amount of Ag in the FICH containing the ^{239}Pu samples and the dummy FICH is probably different, so when subtracting the Ag contribution to both measurements the mentioned deeps appear.

We have made an exhaustive analysis of all sources of uncertainty in the measurement. The results are shown in Figure 23, where the following contributions appear:

- Flux: uncertainty due to the determination of the energy dependency of the neutron fluence.
- ε_f: uncertainty due to the determination of the FICH detection efficiency.
- ε_γ: uncertainty due to the determination of the TAC detection efficiency.
- Sample-out: uncertainty (systematic) due to the subtraction of the sample-out (*dummy*) measurement.
- N. Sens: uncertainty due to the determination of the background induced by the elastic scattered neutrons in ^{239}Pu.
- PFB: uncertainty due to the determination of the post fission background.
- Sys.: total systematic uncertainty (quadratic sum of all the previously mentioned contributions).
- Stat.: uncertainty due to counting statistics.

It may be important to mention that in Figure 23 all the uncertainties appear integrated over certain neutron energy intervals. Some of the contributions may change significantly when integrating in different energy intervals, and in particular when performing resonance analysis.
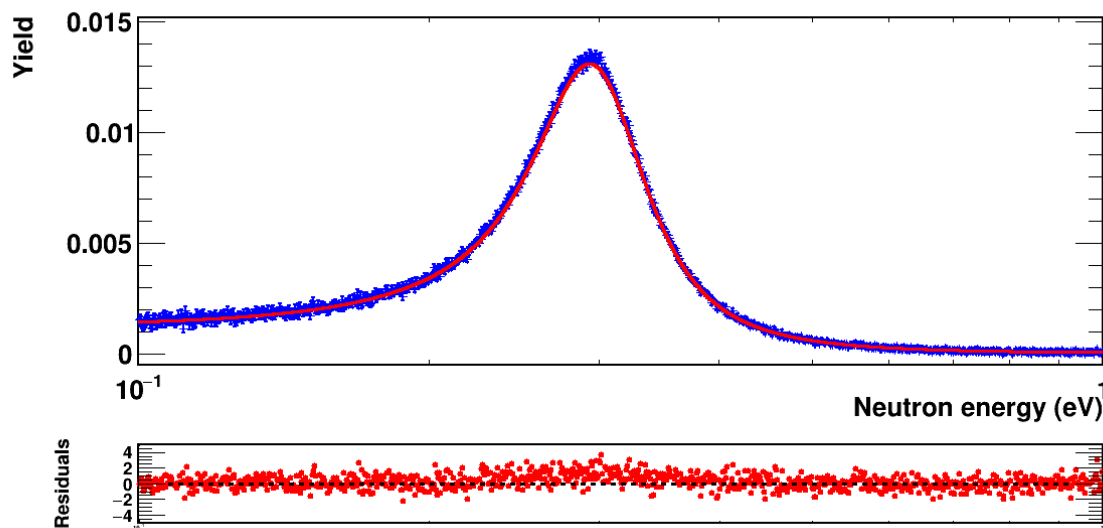

Figure 17: Capture yield obtained in this measurement with the fission tagging configuration, in blue, compared to ENDF/B-VII.1, in red. Residuals are presented in the bottom panel.

22

Figure 18: Capture yield obtained in this measurement with the fission tagging configuration, in blue, compared to ENDF/B-VII.1, in red. Residuals are presented in the bottom panel.
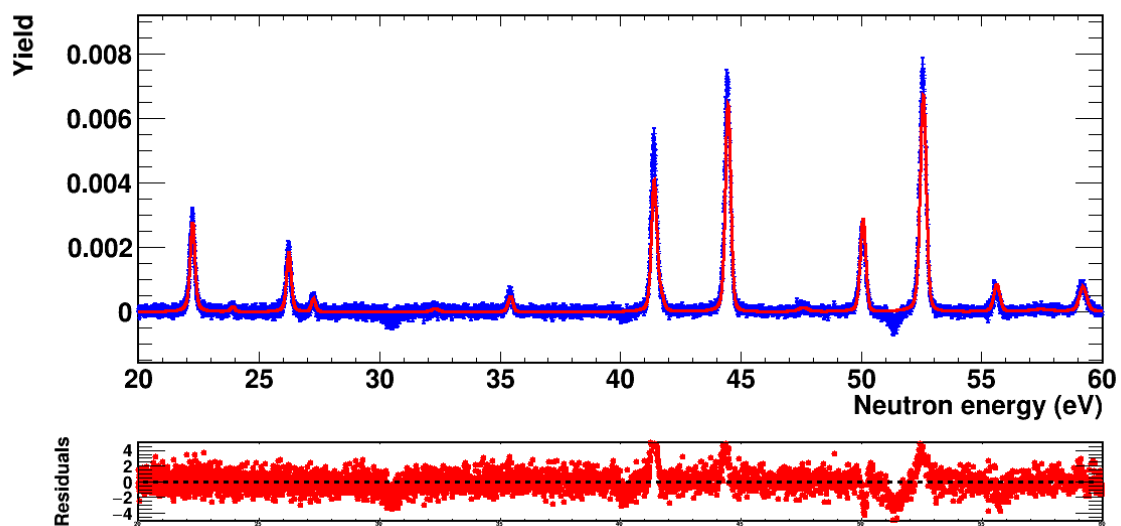
Figure 19: Capture yield obtained in this measurement with the fission tagging configuration, in blue, compared to ENDF/B-VII.1, in red. Residuals are presented in the bottom panel.

Figure 20: Capture yield obtained in this measurement with the fission tagging configuration, in blue, compared to ENDF/B-VII.1, in red. Residuals are presented in the bottom panel.
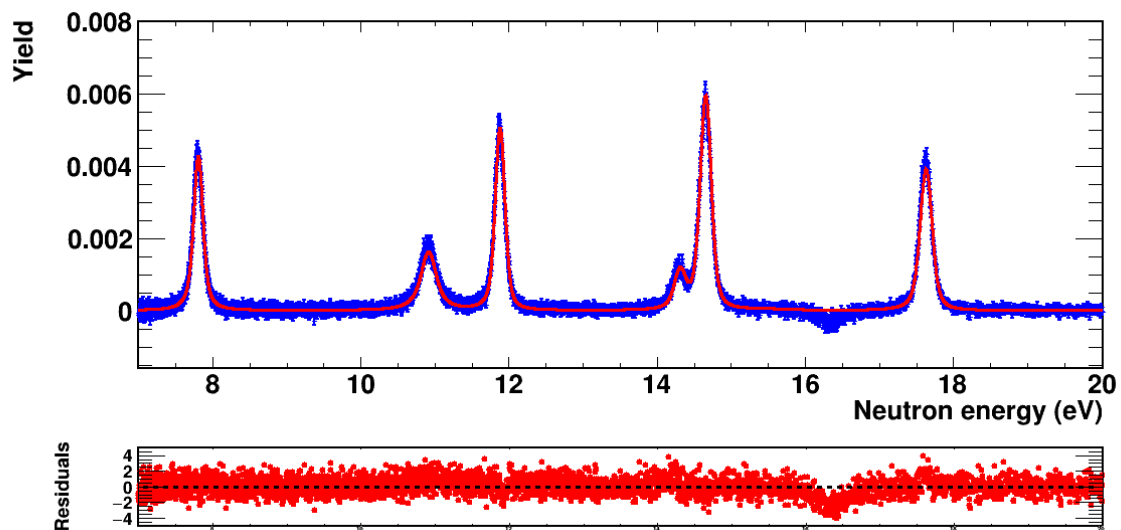

Figure 21: Capture yield obtained in this measurement with the fission tagging configuration, in blue, compared to ENDF/B-VII.1, in red. Residuals are presented in the bottom panel.

24

Figure 22: Capture yield obtained in this measurement with the fission tagging configuration, in blue, compared to ENDF/B-VII.1, in red. Residuals are presented in the bottom panel.
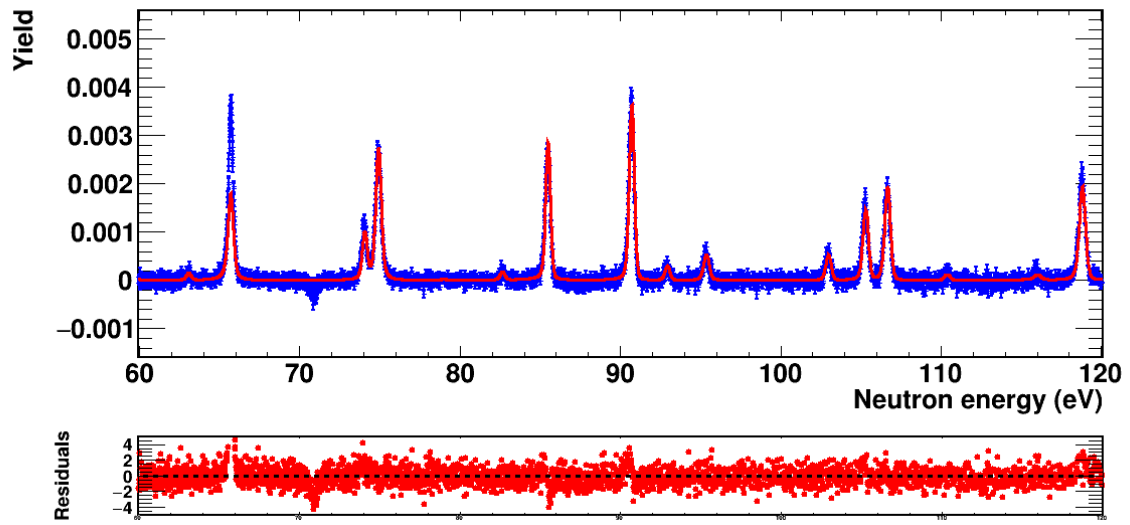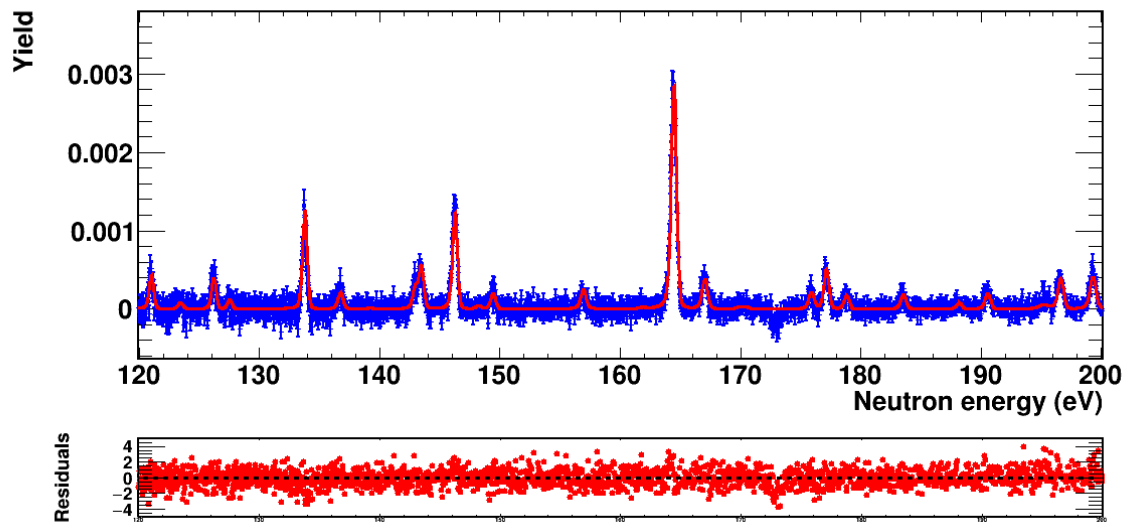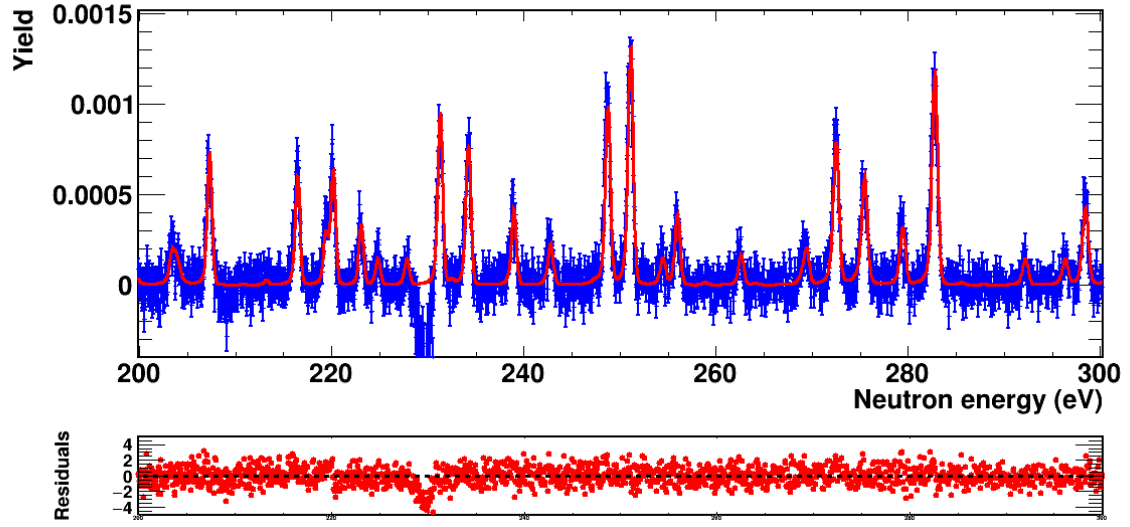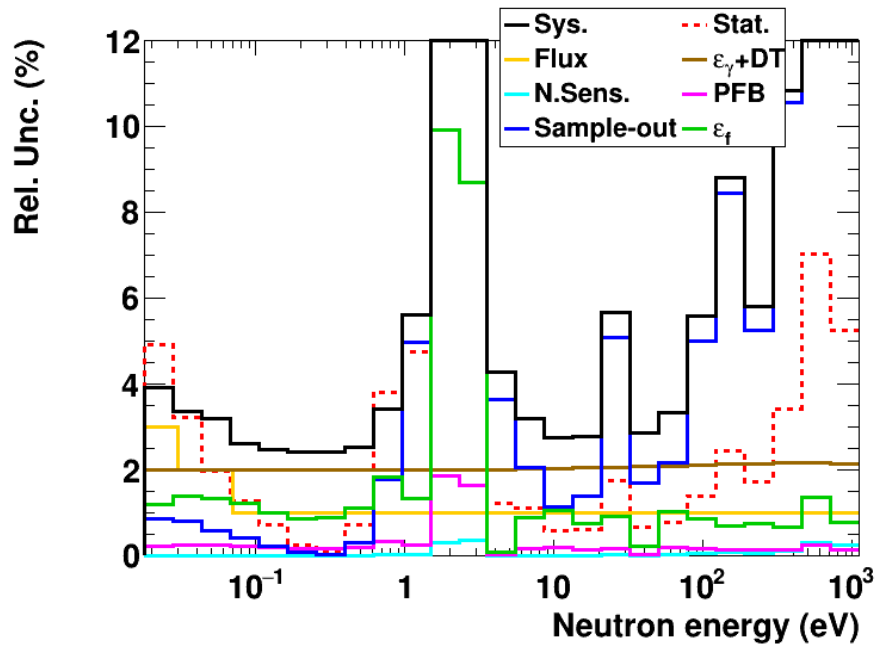

Figure 23: Uncertainties in the ^{239}Pu(n,γ) yield, as a function of the neutron energy.

5 Summary and conclusions

We have performed a new measurement of the ^{239}Pu(n,γ) cross section between 0.02 eV and 10 keV at the n_TOF facility at CERN. The uncertainties achieved (Figure 23) are very similar to those estimated in the preparation of the experiment, which appear in the proposal sent to the scientific committee at CERN (Fig. 3 of [25]). We consider, therefore, that the measurement has achieved the proposed objectives. The results should be analyzed together with the other existing measurements, including all reaction channels. With this, these data will allow to make a better evaluation of the ^{239}Pu cross section, reducing the present uncertainties.

The measured data is publicly available at this link:

https://cernbox.cern.ch/s/DnpEQJwmvlLow5a

6 References

[1] M. Salvatores et al., International Evaluation Co-operation. Volume 26 (OECD Publishing, Paris, 2008) 465.

[2] N. Otuka et al., Nucl. Data Sheets 120, 272-276 (2014)

[3] D.A. Brown, Nucl. Data Sheets 148, 1-142 (2018)

[4] A. Plompen et al., Eur. Phys. J. A 56, 1-108 (2020)

[5] K. Shibata et al., J. Nucl. Sci. Technol. 48, 1046-1051 (2011)

[6] M. B. Chadwick et al., Nucl. Data Sheets 112, 2887 (2011)

[7] E. Dupont et al., EPJ Web Conf. 239, 15005 (2020)

[8] Gwin et al., Nucl. Sci. Eng. 45, 25 (1971)

[9] S. Mosby et al., Phys. Rev. C 89, 034610 (2014)

[10] S. Mosby et al., Phys. Rev. C 97, 041601 (2018)

[11] S. Mosby et al., Nucl. Data Sheets 148, 312-321 (2018)

[12] C. Guerrero et al., Eur. Phys. J. A 49, 27 (2013)

[13] J. Balibrea-Correa et al., Phys. Rev. C 102, 044615 (2020)

[14] M. Bacak, et al., EPJ Web Conf. 239, 01043 (2020)

[15] C. Guerrero et al., Nucl. Instrum. Methods A 608 3, 424-433 (2009)

[16] U. Abbondanno et al., Nucl. Instrum. Methods A 538 1-3, 692-702 (2005)

[17] G. de Saussure et al., Nuclear Data for Reactors: Proceedings of a Conference on Nuclear Data, Microscopic Cross Sections, and Other Data Basic for Reactors (IAEA, Vienna, 1967), 437.

[18] C. Guerrero et al., Phys. Rev. C 85, 044616 (2012).

[19] E. Mendoza et al., Phys. Rev. C 90, 034608 (2014).

[20] S. Agostinelli et al., Nucl. Instrum. Meth. A 506 (2003) 250-303

[21] J. Allison et al., Nucl. Instrum. Meth. A 835 (2016) 186-225

[22] C. Guerrero et al., Nucl. Instrum. Methods A 671 108-117 (2012)

[23] E. Mendoza et al., Nucl. Instrum. Methods A 1047, 167894 (2023).

[24] INDEN - International Nuclear Data Evaluation Network https://www-nds.iaea.org/INDEN/

[25] D. Cano-Ott et al., CERN-INTC-2020-049 ; INTC-P-567 (2020). https://cds.cern.ch/record/2730935

PART II: ^{94,95,96}Mo (n,γ) and (n,tot) measurements

M. Busso[1,2], D. M. Castelluccio[1,3], P. Console Camprini[1,3], N. Colonna[1],
S. Cristallo[1,4], C. Domingo-pardo[5], A. Guglielmelli[1,3], J. Heyse[6], S. Kopecky[6],
C. Lederer-Woods[7], A. Manna[1,8], C. Massimi[1,8], P. Mastinu[1], A. Mengoni[1,3],
P.M. Milazzo[1], R. Mucciola[1,2 (*)], C. Paradela-Dobarro[6], T. Rauscher[9], F. Rocchi[3],
P. Schillebeeckx[6], N. Sosnin[7], N. Terranova[1,3], G. Vannini[1] and the n_TOF
Collaboration[10]

1. Istituto Nazionale di Fisica Nucleare, INFN, Italy

2. University of Perugia- Perugia, Italy

3. Agenzia per le Nuove Tecnologie, l'Energia e lo Sviluppo Economico Sostenibile, ENEA, Italy

4. Istituto Nazionale di Astrofisica, INAF- Teramo, Italy

5. Instituto de Fisica Corpuscular, CSIC- Universidad de Valencia, Spain

6. European Commission, Joint Research Centre, Geel, Belgium

7. School of Physics and Astronomy, University of Edinburgh, United Kingdom

8. Department of Physics and Astronomy, University of Bologna, Italy

9. Department of Physics, University of Basel, Basel, Switzerland

10. www.cern.ch/n_TOF

(*) corresponding author: riccardo.mucciola@cern.ch

7 Introduction to Part II

The neutron cross-section of molybdenum isotopes plays an important role in many different scientific fields ranging from nuclear astrophysics to nuclear technologies. In nuclear astrophysics, traces of molybdenum are found in presolar silicon carbide (SiC) grains, which are produced in the convective envelope of AGB stars. These grains spread, by stellar winds, were involved in the solar system formation and included in pristine meteorites felt on Earth when they have been collected and studied. These grains, therefore, represent a probe to measure the isotopic abundance in the convective envelope of AGB stars where they were formed. Presolar grain abundances can be used as a constraint to test and validate astrophysical models. From comparison of the expected isotopic abundances of molybdenum isotopes calculated by the FRUITY model [1, 2, 3] with the observed composition of several SiC grains, a poor agreement of the content of [95,97,98]Mo was observed. This deviation could be explained by an underestimation of the neutron capture cross-sections of molybdenum isotopes [5].

In nuclear technologies, molybdenum is produced by fission in nuclear power plants. Therefore, an accurate knowledge of its cross-section is needed for safety studies on a burn-up credit approach [6]. In addition, some studies on new generation Accident Tolerant Fuel (ATF) are ongoing. These investigations have been started to increase the resistance of the fuel to extreme events like earthquakes. New generation alloys using Mo could improve the resistance of the fuel while also increasing the resistance to high temperatures [7]. To perform these studies a very accurate knowledge of the neutron capture cross-section of molybdenum is needed. Another application of molybdenum is related to research reactors. These kinds of reactors are smaller than the ones used for power generation and they usually require a high enrichment of uranium to operate. However, the use of low-enriched uranium (LEU) in those kinds of reactors is highly encouraged. To allow the operation of these reactors using LEU, it is necessary to use a mixture of materials in the fuel to change its physical characteristics. One of the main candidates to achieve this objective is the use of UMo alloys which increases the density of the fuel reducing the need for enrichment [8]. Finally, thanks to its thermo-mechanical characteristics molybdenum could be used in future fusion power plants as a replacement for tungsten. The exposure to neutrons inside a fusion reactor can cause activation and thus maintenance and decommissioning problems. The possibility to change the isotopic abundance of the employed molybdenum (biasing) in such applications is under investigation and could lead to a drastic reduction in the long-term radioactivity of the material [9].

8 Experimental setup

8.1 The samples

The samples used in this campaign consist of metallic powders enriched in 94,95,96Mo with an enrichment of each sample is above 95%wt for all the isotopes. The declared isotopic composition of the powders is reported in Table 2.

Sample	^{92}Mo	^{94}Mo	^{95}Mo	^{96}Mo	^{97}Mo	^{98}Mo	^{100}Mo
^{94}Mo	0.63%	98.97%	0.36%	0.01%	0.01%	0.01%	0.01%

95Mo	0.31%	0.69%	95.40%	2.24%	0.51%	0.65%	0.20%
96Mo	0.28%	0.24%	1.01%	95.90%	1.00%	1.32%	0.25%

Table 2: Declared abundances of the enriched molybdenum powders.

The powders were pressed into self-sustained pellets of 2 cm diameter. To avoid any loss of material during transportation and measurements, the samples were sealed under vacuum in thin plastic bags. A picture of one of the pellets in the plastic bag is shown in Figure 24.

Figure 24: Picture of the 95Mo pellet sealed under vacuum in a thin plastic bag.

The details of the samples used in the measurements are reported in Table 3. The areal density of the samples was derived with an uncertainty of 0.1% from a measurement of the weight and the area. The area was determined by an optical surface inspection with a microscope system by Mitutoyo [10]. The area is measured by a computerized microscope system which scans the surface of the sample. By measuring the surface area six different times it is possible to obtain an uncertainty smaller than 0.05%. The samples were used in all the measurements at n_TOF and GELINA.

Sample	Mass (g)	Areal density (atoms/b)
94Mo	1.9526 (3)	$3.960\,(4)\times10^{-3}$
95Mo	1.9745 (3)	$3.954\,(4)\times10^{-3}$
96Mo	1.9175 (3)	$3.806\,(4)\times10^{-3}$

Table 3: Mass and areal densities of the 94,95,96Mo enriched used in the measurements campaigns at n_TOF. The areal density is determined with an uncertainty of 0.1%.

8.2   Description of the experimental setups

The transmission experiments were performed at the 10 m station of flight-path 13 (FP-13) of GELINA, which forms an angle of 18° with the normal to the moderator. For these measurements, the moderated neutron flux was used and, to attenuate the fast neutron component and the intensity of the γ-ray flash, a shadow bar made of Cu and Pb was placed close to the neutron production target.

The detector used for the transmission measurements is a rectangular scintillator produced by Scionix [11]. The scintillator is enriched to 95% in ^{6}Li and it is enclosed in an aluminum canning surrounded by a solid μ-metal shield placed in a metal "castle" to reduce the effect of scattered neutrons. A picture of the glass scintillator is shown in Figure 25.
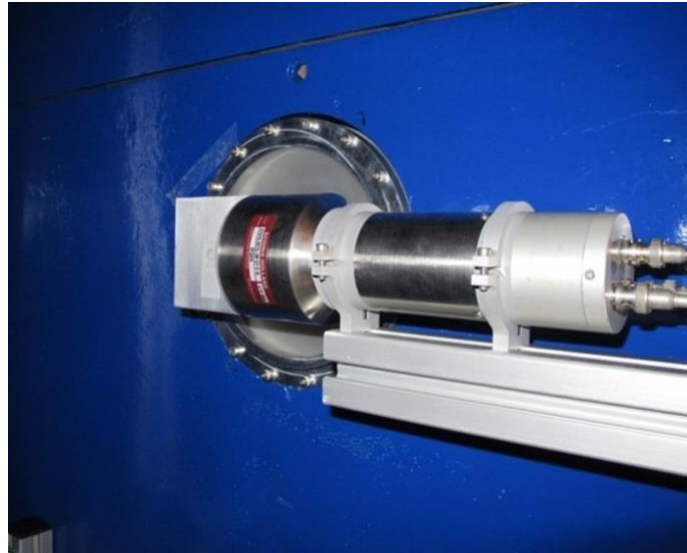

Figure 25: Picture of the Li-glass scintillator used at the 10 m station of GELINA for transmission measurements.

The capture measurements were performed in both experimental areas of n_TOF: EAR1, located at 185 m from the neutron producing target, and EAR2, located at 19 m from the spallation target.

The experimental setup used in the measurement campaign in EAR1 consists of four C_6D_6 detectors developed at the Legnaro laboratory. These liquid scintillator detectors were optimized for neutron capture measurements to achieve le smaller sensitivity to neutron possible. In addition, the small gamma detection efficiency makes these detectors suitable for the use of the Total Energy Detection technique.

The detectors were placed at 9 cm from the center of the samples at a 135° angle backwards with respect to the beam. The samples were mounted on an automatic sample exchanger together with all the additional samples needed for background and normalization i.e. carbon, lead, gold, and empty. A dummy sample consisting of a plastic bag identical to the one used to contain the pellets was also put in the sample exchanger to estimate the background.

The samples were measured also at the second experimental area of n_TOF, EAR2. During this campaign, a total of 8 STED detectors were used together with 2 Legnaro C_6D_6 detectors and a newly developed scintillator consisting of a crystal of deuterated stilbene (DSTI). All the STED and the DSTI detectors were very close to the sample position, at 6 cm from the sample center at a 90° angle with respect to the beam. The two C_6D_6 detectors were placed further away, at around 20 cm, to reduce the noise induced by the γ flash and other γ-rays in the beam line. These detectors were placed at a 135° angle backwards with respect to the beam. A picture of the two experimental setup is shown in Figure 26.
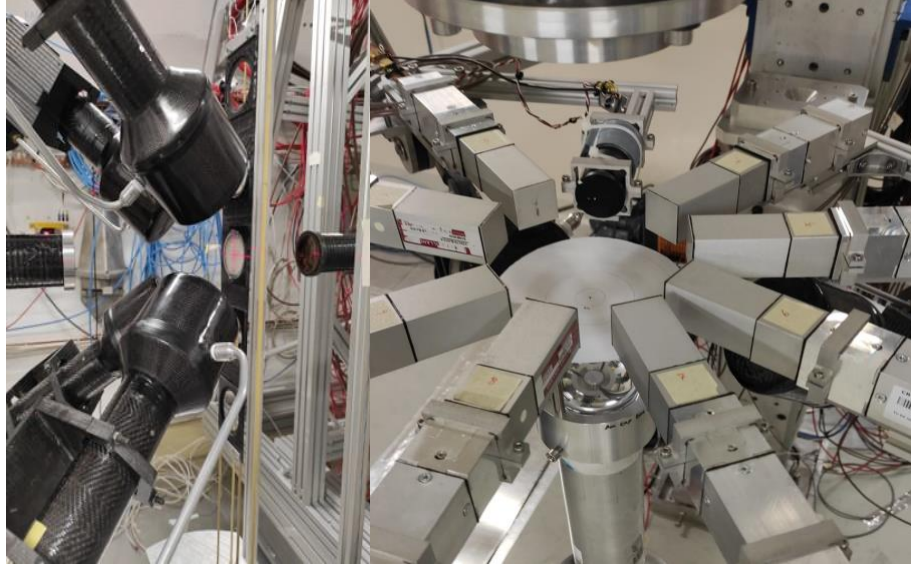
Figure 26: Picture of the detection setup used in EAR1 (left) and EAR2 (right).

9 Analysis of transmission data

The transmission spectra of a sample is obtained as a ratio of the counts with the sample in the beam (Cin) and the ones without the sample (C_out). Both spectra have been corrected for their background contribution:

$$T_{exp} = N_T \frac{C_{in} - K B_{in}}{C_{out} - K B_{out}}$$

9.1 Data reduction

The data reduction procedure to obtain T_{exp} has been performed using the AGS (Analysis of Geel Spectra) developed at the IRMM [12, 13]. This package was used for dead-time correction, background fitting and subtraction, and normalization. The program allows a full propagation of the uncertainty starting from the uncorrelated uncertainty due to counting statistics. The experimental transmission obtained with AGS includes a complete covariance matrix with correlated and uncorrelated uncertainty.

Both sample-in and sample-out spectra have been corrected by the deadtime of the detection and acquisition systems. The dead-time has been estimated from the time distance of two consecutive acquired events. The dead time correction is based on the Moore formula [14] and it accounts for possible variations of neutron beam intensity. The normalization factor N_T accounts for the integrated intensities of the neutron beam in sample-in and sample-out configurations.

Since both the neutron flux intensity and energy profile vary during the campaign, the sample-in and sample-out measurements have been divided into short duration cycles of around 600 s alternating between the different configurations. This procedure reduces the uncertainty on the normalization to less than 0.25% [15]. A normalization factor of N_T = 1.0000(25) was therefore included in Eq. 1 to account for this uncertainty. All the spectra were normalized to the same bin-width and the neutron intensity in the target hall. The latter was measured using the BF3 monitors placed in different

positions in the target hall. The flight-path length of L = 10.860(1) m was obtained from previous measurements with 238U using the reference resonance at 6.673 eV [16].
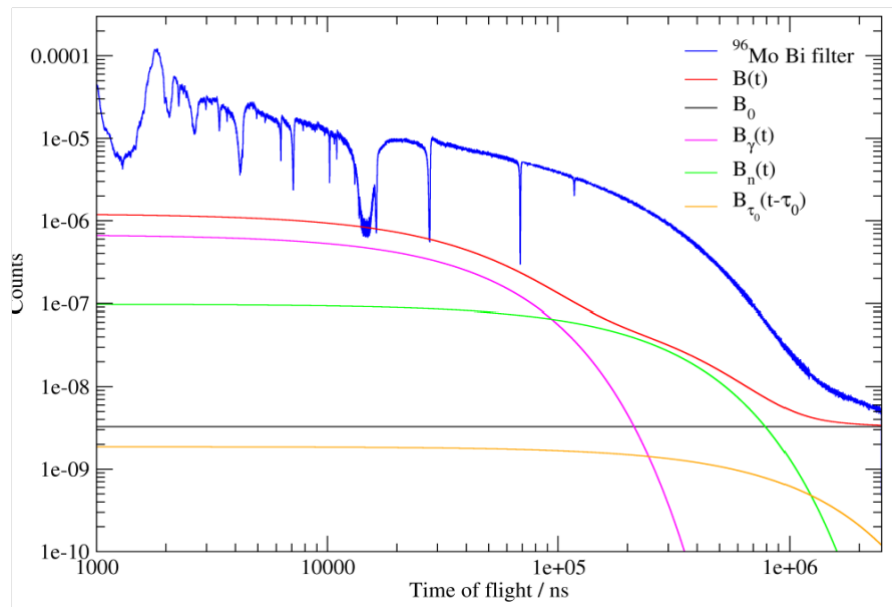
9.2   Background

The background of both sample-in and sample-out configurations have been parameterized using an analytical function:

$$B(t) = B_0 + B_\gamma(t) + B_n(t) + B_{\tau 0}(t + \tau_0).$$

The first component B_0 is the ambient radiation background and any other time-independent contributions. The term B_γ is related to the detection of the 2.2 MeV γ-rays emitted by the hydrogen in the beam moderator. Lastly, Bn accounts for the neutrons scattered inside the detection station while Bτ0 is attributable to the slow overlap neutron from previous accelerator cycles. The shape of the background i.e. the free parameters of the analytical expression were obtained from runs with additional filters. The level of the background was monitored using the 132 eV black resonance of cobalt.

The time dependence of the background was obtained using the black resonance technique. Therefore, specific runs with Na (2850 eV), Co (130 eV), W (21.1 eV), and Ag (5.2 eV) black resonance filters in the beam have been carried out to accurately determine the background shape in the entire energy range of interest. The background level in the sample-in and sample-out measurements were obtained by scaling this background to match the counts obtained at the bottom of the permanent black resonance filters. The permanent filters were Na and Co or Na and Bi. The Bi filter was used to avoid the black resonance of Co at 132 eV which covers one of the main resonances of ^{96}Mo. An example of the estimated background and all its different components can be found in Figure 27 for ^{96}Mo sample-in with Bi fixed filter.

Figure 27: Dead-time corrected TOF-spectra resulting from transmission measurements with the ^{96}Mo sample-in measurement at the 10 m station of GELINA with fixed Na and Bi black filters. The total background together with the time independent and time-dependent background components are shown.

10 Analysis of capture data

Two different sets of capture measurements were performed at the n_TOF neutron time-of-flight facility, one at EAR1 and the other at EAR2. Even though the measurements were performed in two different experimental areas with different experimental setups, the analysis procedure used for both set of measurements is exactly the same and it will be described here.

10.1 Pulse Shape Analysis

The raw signals obtained from all the detectors were stored in CASTOR (CERN Advanced STORage manager), the data archive of CERN. These data were processed using the PSA (Pulse Shape Analysis) [17] developed by the n_TOF Collaboration. The routine provides amplitude and timing for all the recorded signals while calculating the baseline after each signal taking into account the effect of the tail thus it manages to resolve pile-up events. For each detector, an accurate study of the shape of the signals has been carried out to accurately reconstruct them in the PSA routine. An example of the signal reconstructed by the PSA routine is shown in Figure 28.
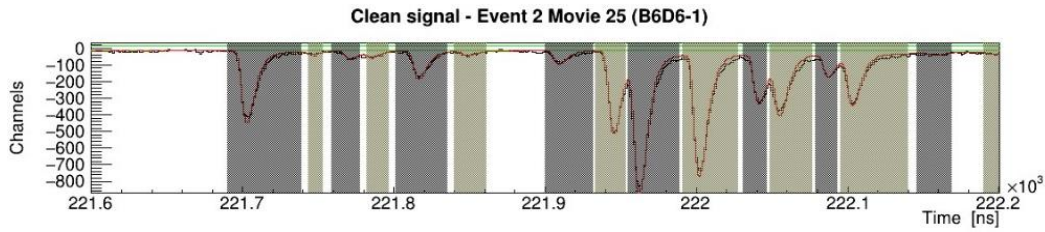

Figure 28: Raw data (black) and reconstructed baseline (green) and signals (red) obtained with the PSA routine. The grey areas represent the integrate range of each reconstructed signal.

10.2 Calibration

A set of measurements using γ-emitting radioactive sources was carried out in order to calibrate the detectors. The calibration sources used in this campaign are ^{137}Cs (661 keV), ^{88}Y (898, 1836 keV), and AmBe (4438 keV). The calibration measurement was performed once per week throughout the experimental campaign to monitor the stability of the detectors. No appreciable deviations was observed during both experimental campaigns therefore it can be said that the detectors had a stable behavior in both EAR1 and EAR2. The calibrations were performed by comparing Monte Carlo simulations of the detection setup performed with the calibration sources in the sample position with the experimental data. The effect of the energy resolutions of the detectors was convoluted with the results of the simulations. A comparison of the measured spectra with calibrations sources and the results of the Monte Carlo simulations is showed in Figure 29.
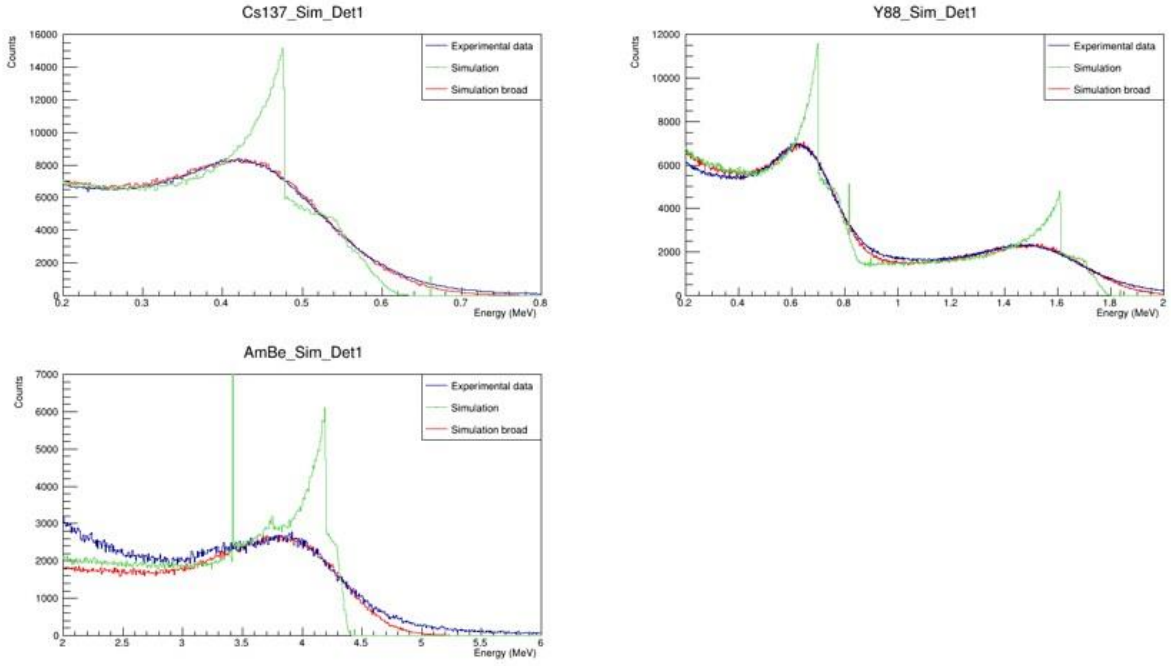
Figure 29: Comparison of the experimental data obtained with the calibration sources (blue) with the results of the Monte Carlo simulations (green). The results of the simulations convoluted with the energy resolution of the detectors is also showed (red).

10.3 Weighting functions

The capture cross-section measurements at n_TOF follow the principle of the total energy detection technique. This technique requires capture detectors with a low detection efficiency and a proportionality between the deposited energy and the efficiency. One way to obtain such proportionality is the use of the so-called Weighting Functions (WF). To obtain accurate WF a very accurate knowledge of detector response for different γ-ray energies is required. This response depends on γ-rays transportation both in the detection system and within the sample itself, and it has been simulated using GEANT4 [18] Monte Carlo code. All the detectors have been accurately reconstructed and positioned to properly reproduce the experimental setup response to γ-rays emitted by the sample. To simulate the response of the detectors to the γ-rays emitted by the samples, γ-rays of varying energy ranging from 100 keV to 15 MeV were generated isotopically inside the samples. The energy deposited in the active volume of each detector was recorded in each run. A total of 10^6 γ-rays were simulated for each energy. The weighting function is defined as:

$$\int_0^\infty R_d(E_d, E_\gamma)W(E_d)dE_d = kE_\gamma$$

where $R_d(E_d, E_\gamma)$ is the detector response, namely the probability of having a deposited energy Ed caused by a γ-ray with Eγ energy. Using the simulation results it was then possible to estimate the Weighting function for all the enriched samples and the gold one. The plot of the weighting function obtained for the Mo samples for the EAR1 campaign is reported in Figure 30.
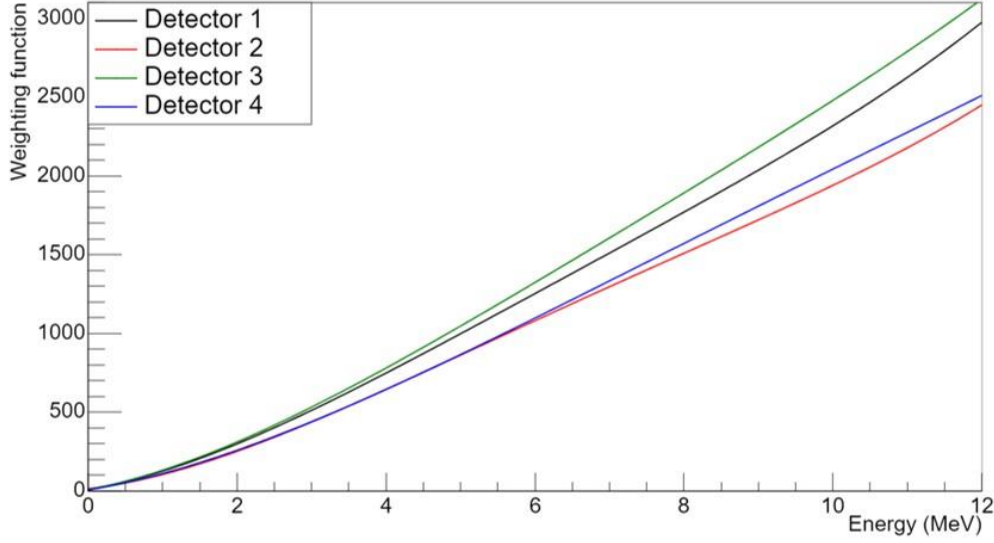
Figure 30: Weighting function of the EAR1 measurement setup obtained from Monte Carlo simulations for the four C_6D_6 detectors.

10.4 Background

The background of a capture measurement is obtained with additional measurements performed to study its components:

Time independent background It is caused by the environmental background and it is estimated by measurements performed with the beam-off and without the sample.

Beam induced background It is caused by the interaction of the beam with other materials in the experimental area and it is estimated with measurements performed with an empty or dummy sample. In this experimental campaign, it was evaluated with a dummy sample consisting of an empty aluminum can identical to the ones used for the samples.

Neutron scattered by the sample Signals due to neutrons scattered by the sample which can in fact later be captured or undergo inelastic reactions in the material of the detector and experimental area. It is evaluated with samples with very low capture cross-section and high scattering cross section like carbon.

In-Beam gamma-rays This background component is caused by the signals generated by the scattering of gamma-rays traveling in the beam together with neutrons. It can be evaluated using a target with a high Z, and therefore a high gamma-ray scattering cross section like lead.

The background is expressed as:

$$B = a_0 + C_{w,Dummy} + R_n(C_{w,C} - C_{w,Empty}) + R_g(C_{w,Pb} - C_{w,C}),$$

where $C_{w,Dummy}$ are the weighted counts obtained with the dummy sample, $C_{w,C}$ and $C_{w,Pb}$ are the counts with the carbon and lead sample, respectively while $C_{w,Empty}$ are the counts without any sample in the beam. The factor R_n accounts for the difference in the scattering yield between the carbon sample and the sample under investigation while R_g accounts for the difference in atomic number between lead and the sample. The measured spectrum for the three molybdenum isotopes together with the

different background components obtained from the additional measurements are shown in Figure 31, Figure 32, and Figure 33.
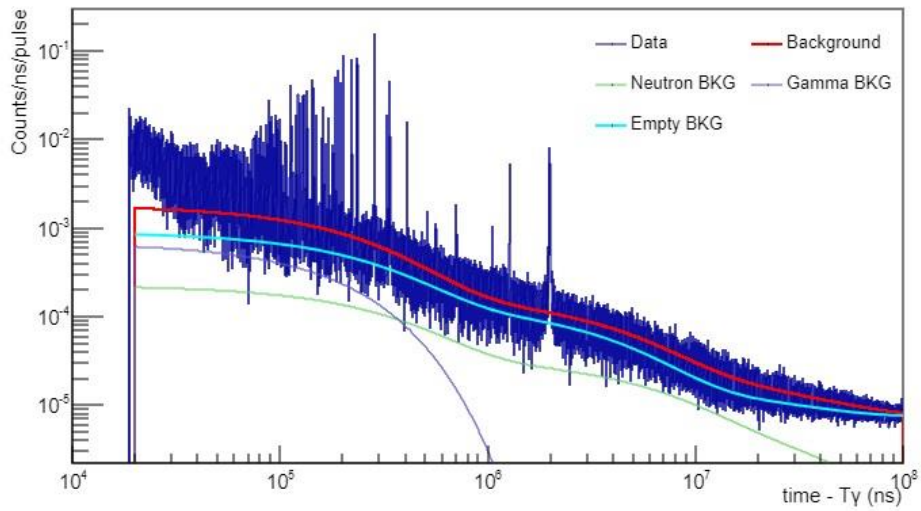

Figure 31: Weighted counts for the ^{94}Mo sample measured at EAR1 together with the different background components.
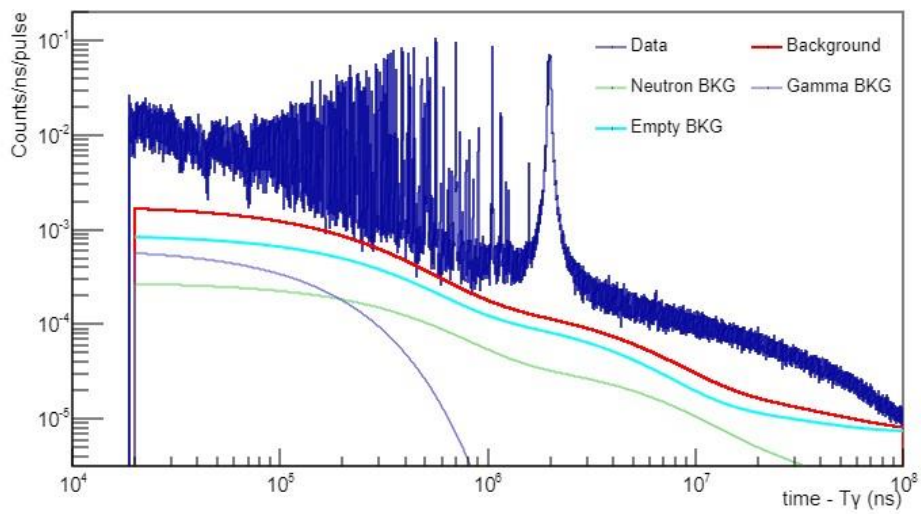

Figure 32: Weighted counts for the ^{95}Mo sample measured at EAR1 together with the different background components.
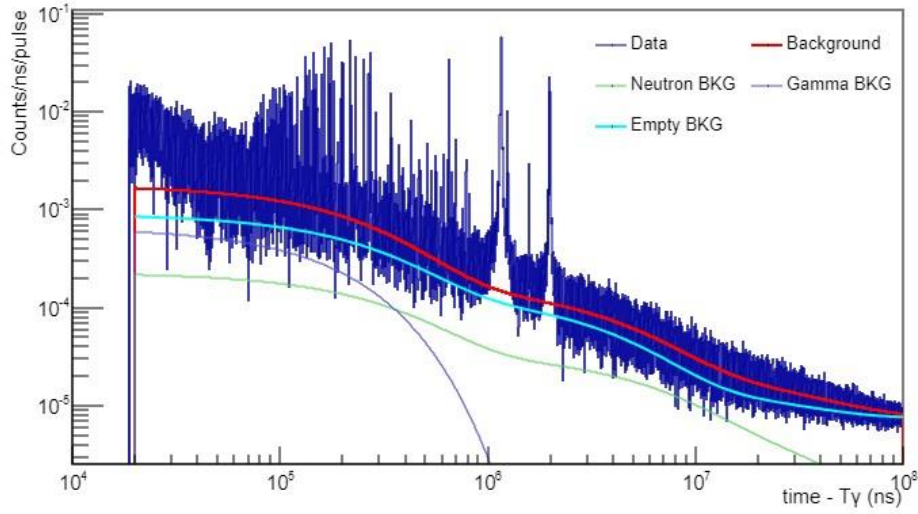
Figure 33: Weighted counts for the ^{96}Mo sample measured at EAR1 together with the different background components.

10.5 Capture yield

After applying all the needed corrections to the capture spectra, the capture yield was obtained, which is defined as:

$$Y_{exp}(E_n) = \frac{C_i(E_n) - B_i(E_n)}{\epsilon} \frac{1}{f\varphi(E_n)}$$

where $C_i(E_n)$ are the counts obtained with the sample in the beam, $B_i(E_n)$ is the background, ϵ is the detection efficiency, $\varphi(E_n)$ is the neutron flux as a function of energy, and f is the beam interception factor of the sample. Both f and ϵ do not depend on the energy of the impinging neutrons. In first approximation, the beam interception factor depends only on the dimension of the sample and it is around 0.7 for 2 cm diameter samples as the ones used in this campaign. Using the weighting functions, we obtain that the efficiency ϵ is proportional to the energy of the cascade, which in turn it is equal to the sum of the separation energy S_n and the energy of the impinging neutron E_n. Since S_n is larger than few MeV for most isotopes (7.37, 9.15, and 6.82 MeV for ^{94,95,96}Mo respectively) at low energy the efficiency can be considered independent of the neutron energy. The energy-independent factors are usually combined in the normalization factor N. The yield can then be expressed as:

$$Y_{exp}(E_n) = N\frac{C_i(E_n) - B_i(E_n)}{\varphi(E_n)}.$$

The normalization factor N can be obtained from a saturated resonance with $\Gamma\gamma \gg \Gamma n$. This kind of resonances have a yield close to 1 and are therefore ideal candidates to obtain the normalization factor. The first resonance of ^{197}Au at 4.9 eV is suitable to calculate the normalization having a $\Gamma\gamma/\Gamma n$ ratio of around 8 and it is saturated for a sample thickness of 0.1 mm, which is the one used in these measurement campaigns. The use of a very thin sample reduces the effect of multiple scattering in the sample. The yield of the gold sample has been obtained with the same procedure described for the Mo samples. The normalization factor was calculated using the R-Matrix code SAMMY [19]. The ^{197}Au resonance parameters reported in the ENDF/B-VIII library have been used for the calculation.

The experimental yield can be related directly to the cross section of the isotope under analysis. The yield is related to the capture cross section with the following equation:

$$Y_{th}(E_n) = (1 - e^{-n\sigma_{tot}})\frac{\sigma_\gamma}{\sigma_{tot}}$$

11 Results

The capture yield for all the enriched molybdenum samples obtained in both experimental areas of n_TOF has been obtained in addition to the transmission spectra obtained at GELINA. The yields and transmission spectra have been analyzed using the R-matrix program SAMMY [19] to obtain the resonance parameters in the full resolved resonance region. The cross section of the different isotopes can be accurately reconstructed using these resonance parameters in the entire energy range of interest. The experimental yields and transmission spectra for the tree isotopes compared with the calculation of SAMMY using the data in the latest version of the JENLD library [20] and the results of the fit for are shown in Figure 34, Figure 35, and Figure 36. A close up on the 1500 eV resonance of 94Mo is showed in Figure 37.

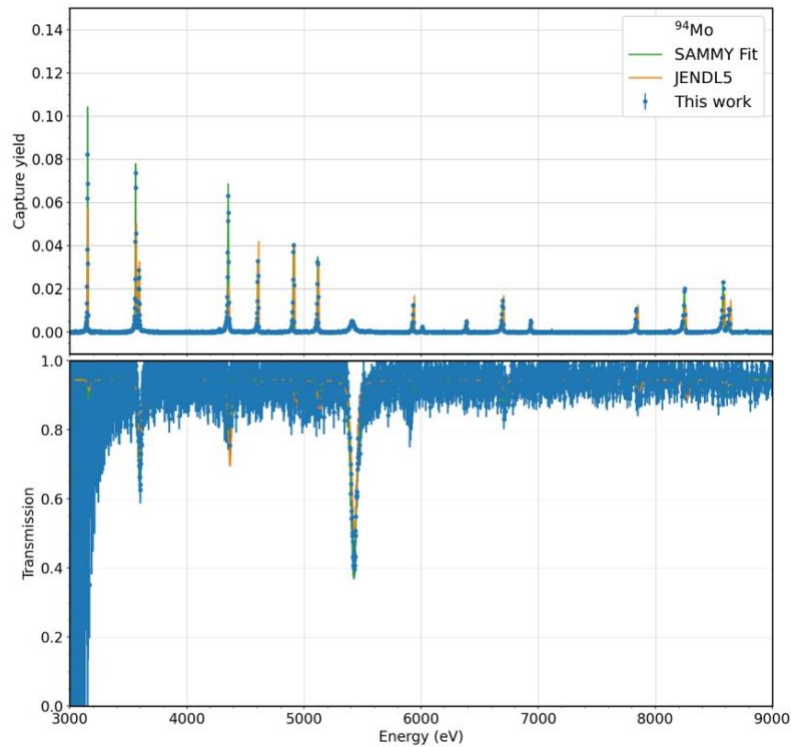**Figure 34: Experimental yield (top) and transmission spectra (bottom) obtained for the ^{94}Mo compared with the calculations performed with SAMMY using the data in JENDL5 (orange) and the fitted values (green).**

Figure 35: Experimental yield (top) and transmission spectra (bottom) obtained for the ⁹⁵Mo compared with the calculations performed with SAMMY using the data in JENDL5 (orange) and the fitted values (green).
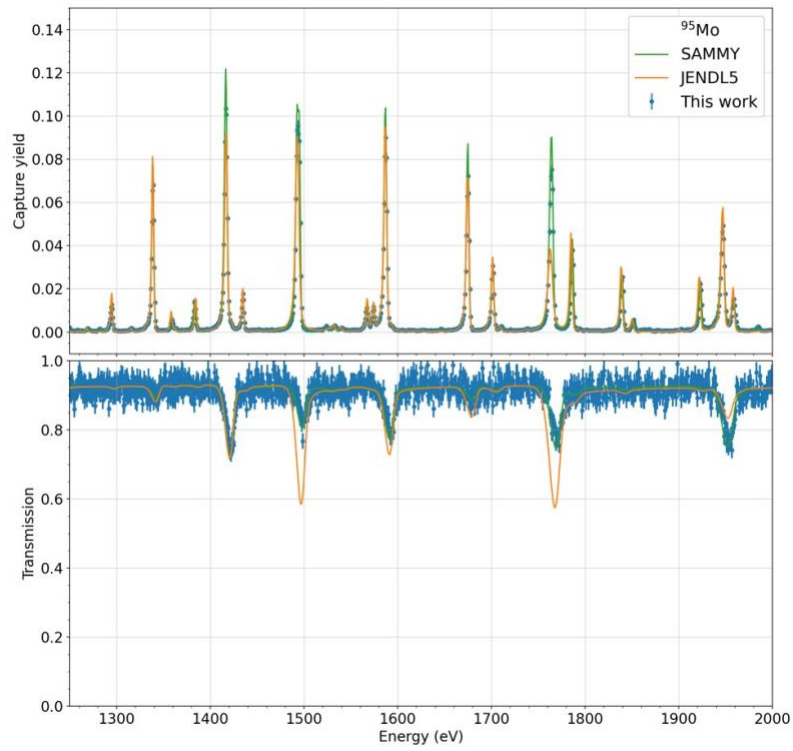

Figure 36: Experimental yield (top) and transmission spectra (bottom) obtained for the ⁹⁶Mo compared with the calculations performed with SAMMY using the data in JENDL5 (orange) and the fitted values (green).

Figure 37: Experimental yield (top) and transmission spectra (bottom) obtained for the ^{94}Mo compared with the calculations performed with SAMMY using the data in JENDL5 (orange) and the fitted values (green) for the 1500 eV resonance.
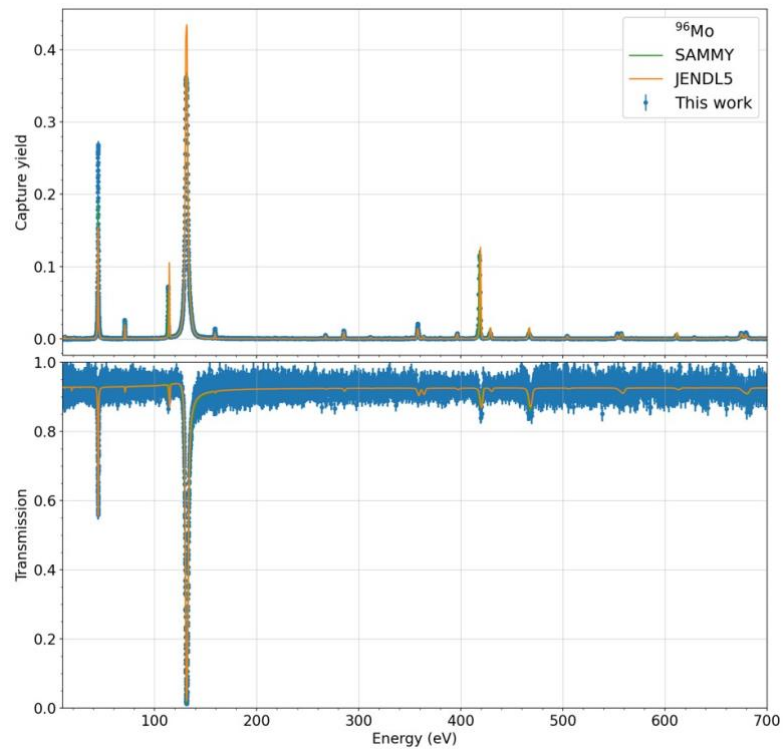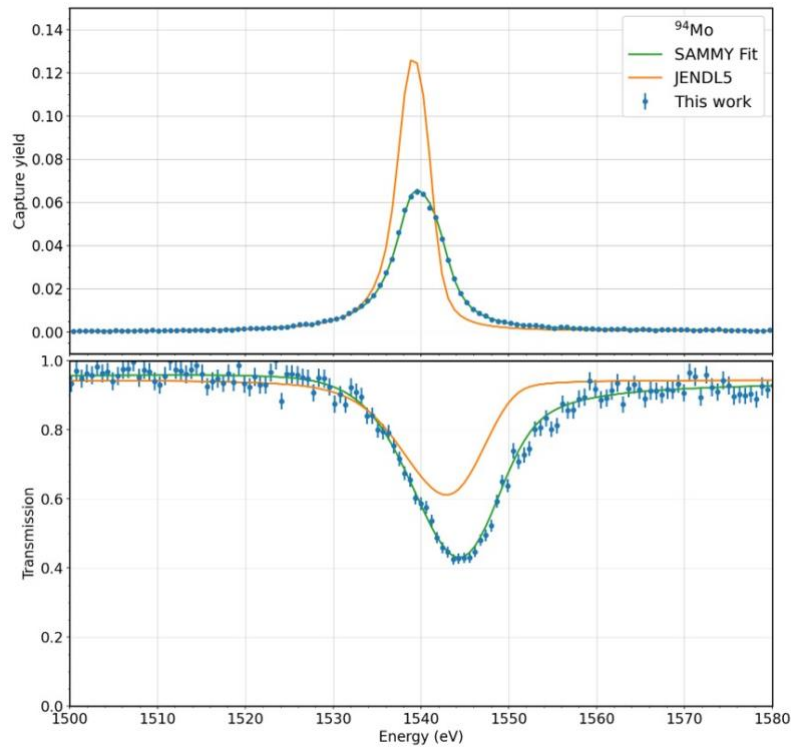
12 Summary

We have performed a series of neutron capture cross section measurements on three molybdenum isotopes ^{94,95,96}Mo at the n_TOF time-of-flight facility at CERN. The results show an improvement in the data description with respect to the data currently present in the latest version of the evaluated libraries, in addition the number of existing resonances was increased for all the isotopes. These data, together with the transmission measurements performed with the same sample at GELINA will allow to produce a better evaluation of the neutron interaction cross section of molybdenum isotopes thus improving the present uncertainties. We can therefore consider the measurements successful.

The measured data is publicly available at this link:

https://cernbox.cern.ch/s/imboKYQXksZYYm0

13 References

[1] S. Cristallo, O. Straniero, R. Gallino, L. Piersanti, I. Dominguez, M. Lederer, The Astrophysical Journal **696** (2009) 797–820.

[2] S. Cristallo, L. Piersanti, O. Straniero, R. Gallino, I. Domınguez, C. Abia, G. D. Rico, M. Quintini, S. Bisterzo, The Astrophysical Journal Supplement Series **197** (2011) 17.

[3] S. Cristallo, O. Straniero, L. Piersanti, D. Gobrecht, The Astrophysical Journal Supplement Series **219** (2015) 40.

[4] I. Dillmann, R. Plag, F. Kappeler, T. Rauscher, Proceeding of the workshop EFNUDAT Fast Neutrons (2009).

[5] N. Liu, T. Stephan, S. Cristallo, R. Gallino, P. Boehnke, L. R. Nittler, C. M. O. Alexander, A. M. Davis, R. Trappitsch, M. J. Pellin, I. Dillmann, ApJ **881** (2019) 28.

[6] I. Gauld, G. Ilas, G. Radulescu, Technical Report NUREG/CR-7012, US Nuclear Regulatory Commission (2011).

[7] B. Cheng, Y. Kim, P. Chou, Nucl. Eng. Tech. **48** (2016) 16–25.

[8] X. Iltis, H. Palancher, J. Allenou, F. Vanni, B. Stepnik, A. Leenaers, S. V. D. Berghe, D. Keiser, I. Glagolenko, EPJ Nuclear Sci. Technol. **4** (2018) 49.

[9] M. Gilbert, L. Packer, T. Stainer, Nuclear Fusion **60** (2020) 106022.

[10] https://www.mitutoyo.co.jp/eng/ (03/06/2016).

[11] https://scionix.nl/.

[12] B. Becker, C. Bastian, J. Heyse, S. Kopecky, P. Schillebeeckx, NEA/DB/DOC (2004) 4.

[13] B. Becker, C. Bastian, F. Emiliani, F. Gunsing, J. Heyse, K. Kauwenberghs, S. Kopecky, C. Lampoudis, C. Massimi, N. Otuka, P. Schillebeeckx, I. Sirakov, J. of Instrumentation **7** (2012) P11002.

[14] M.S.Moore, Nucl. Instr. Meth. **169** (1980) 245.

[15] S. Kopecky, B. Becker, J. Drohe, N. Otuka, P. Schillebeeckx, D. Vendelbo, R. Wynants, Publications Office of the European Union (2013) JRC86941.

[16] H. Derrien, et al., ORNL/TM-2005/241, Oak Ridge National Laboratory, Oak Ridge (2005).

[17] P. Zugec, et al., Nucl. Inst. Meth. A **812** (2016) 134–144.

[18] S. Agostinelli, et al., Nucl. Inst. Meth. A **506** (2003) 250–303.

[19] N. M. Larson, ORNL/TM-9179/R8 ENDF-364/R2 (2008).

[20] K. Shibata, O. Iwamoto, T. Nakagawa, N. Iwamoto, A. Ichihara, S. Kunieda, S. Chiba, K. Furutaka, N. Otuka, T. Ohsawa, T. Murata, H. Matsunobu, A. Zukeran, S. Kamada, J. Katakura, J. Nucl. Sci. Tech. **48** (2011) 1–30.